JGR Solid Earth

RESEARCH ARTICLE
10.1029/2023JB027894

Mélange Signatures and Low Oxygen Fugacity in Eclogite Xenoliths From the Crust-Mantle Transition Below a Mesoproterozoic Collision Belt

Sonja Aulbach[1,2], Heidi E. Höfer[1], Axel Gerdes[1,2], Christel Tinguely[3], and Anton le Roex[3]

[1]Institut für Geowissenschaften, Goethe-Universität Frankfurt, Frankfurt am Main, Germany, [2]Frankfurt Isotope and Element Research Center (FIERCE), Goethe-Universität Frankfurt, Frankfurt am Main, Germany, [3]Department of Geological Sciences, University of Cape Town, Rondebosch, SouthAfrica

Key Points:

- Eclogite xenoliths sampling deep crust-mantle transition below Namaqua-Natal Fold Belt have plagioclase-rich oceanic protoliths
- Enriched xenoliths show signatures of interaction with siliceous, subducted sediment-derived fluids under shallow fore-arc conditions
- Fe^{3+}-based eclogite oxybarometry with oxygen fugacities below sulfate stability limits the role of S^{6+} species in mantle wedge oxidation

Supporting Information:

Supporting Information may be found in the online version of this article.

Correspondence to:

S. Aulbach,
s.aulbach@em.uni-frankfurt.de

Citation:

Aulbach, S., Höfer, H. E., Gerdes, A., Tinguely, C., & le Roex, A. (2024). Mélange signatures and low oxygen fugacity in eclogite xenoliths from the crust-mantle transition below a Mesoproterozoic collision belt. *Journal of Geophysical Research: Solid Earth*, *129*, e2023JB027894. https://doi.org/10.1029/2023JB027894

Received 20 SEP 2023
Accepted 15 JAN 2024

Author Contributions:

Conceptualization: Sonja Aulbach
Formal analysis: Sonja Aulbach, Heidi E. Höfer, Axel Gerdes
Funding acquisition: Sonja Aulbach
Investigation: Sonja Aulbach, Heidi E. Höfer, Axel Gerdes
Methodology: Sonja Aulbach, Heidi E. Höfer, Axel Gerdes
Project administration: Sonja Aulbach
Resources: Heidi E. Höfer, Axel Gerdes, Christel Tinguely, Anton le Roex
Validation: Heidi E. Höfer, Axel Gerdes
Visualization: Sonja Aulbach

Abstract Mass transfer across the crust-mantle boundary is a fundamental process governing planetary differentiation, the evolution of geochemical reservoirs and ore formation, controlled by physicochemical conditions at the crust-mantle interface. In situ trace-element, clinopyroxene $^{87}Sr/^{86}Sr$ and garnet $Fe^{3+}/\Sigma Fe$ of kimberlite-borne eclogite xenoliths from the deep (~50 km) crust-mantle transition below the ca. 1.2–1.0 Ga Namaqua-Natal Fold Belt (southwestern Kaapvaal craton margin) were determined to elucidate their origin and evolution, and to constrain the oxygen fugacity of this pivotal but largely inaccessible environment. Based on a garnet source signature (NMORB-normalized Er/Lu > 1) in pristine "gabbroic" eclogites with pronounced positive Eu, Sr, and Pb anomalies, the suite is interpreted as originating as plagioclase-rich cumulates in oceanic crust from melts generated beneath mature oceanic lithosphere, subsequently subducted during the Namaqua-Natal orogeny. Enriched eclogites have higher measured $^{87}Sr/^{86}Sr$ in clinopyroxene (up to 0.7054) than gabbroic ones (up to 0.7036), and show increasing bulk-rock Li, Be and Pb abundances with increasing $\delta^{18}O$ in clinopyroxene, and muted Eu-Sr-Pb anomalies. These systematics suggest interaction with a siliceous fluid sourced from seawater-altered oceanic sediment in a subduction mélange setting. Garnet $Fe^{3+}/\Sigma Fe$ in deep crustal eclogites is extremely low (0.01–0.04, ±0.01 1σ), as inherited from the plagioclase-rich cumulate protolith, and owing to preferred partitioning into clinopyroxene at low temperatures (~815–1000°C). Average maximum oxygen fugacities ($\Delta \log fO_2$(FMQ) = −3.1 ± 1.0 to −0.5 ± 0.7 relative to the Fayalite-Magnetite-Quartz buffer) are higher than in deeper-seated on-craton eclogite xenoliths, but mostly below sulfate stability, limiting the role of S^{6+} species in oxidizing the mantle wedge.

Plain Language Summary Subduction zones represent the main interface between Earth's surface and its deep interior. Metamorphic reactions during subduction cause fluid or melt loss from seawater-altered oceanic crust and sediment, which enriches the overlying mantle, and possibly oxidizes it. This would explain why the mantle sources of subduction zone magmas appear to be more oxidized than in other tectonic settings. However, the details of the mass transfer in this deep environment are difficult to constrain because it is inaccessible. Using rare deep-seated magmas (kimberlites) as probes of a ca. 1.2 billion year old southern African subduction zone, we investigated eclogite fragments that originated as subducted oceanic crust and were much later plucked from the wallrocks by the ascending magma. These eclogites show elemental and isotopic signatures of interaction with subducted sediments, pointing to mingling processes similar to those observed in modern subduction zones. We also estimated their oxygen fugacity, a measure of the chemical potential of oxygen. We find that sulfur, which has been implicated in mantle oxidation, would have only been stable in these rocks in its reduced form, making even seawater-altered eclogites sinks rather than sources of oxygen, with implications for the transfer of sulfur-loving metals across the mantle-to-crust-boundary.

1. Introduction

Mantle eclogite and pyroxenite xenoliths form a significant portion of kimberlite-borne xenolith suites worldwide and are often interpreted as metamorphosed equivalents of various parts of subducted oceanic crust that has lost a partial melt during subduction (e.g., Ireland et al., 1994; Jacob, 2004; Smart et al., 2014; Tappe et al., 2011). Craton margins affected by collisional tectonics represent lithospheric weak zones, which protect cratonic interiors by localizing deformation (Lenardic et al., 2003) and are subsequently exploited as pathways by enriched melts, such as kimberlites (e.g., Tappe et al., 2020), which are potent metasomatic agents also in eclogite

Writing – original draft: Sonja Aulbach
Writing – review & editing: Heidi E. Höfer, Christel Tinguely, Anton le Roex

(e.g., Aulbach, Massuyeau, et al., 2020; Fitzpayne et al., 2020). As a consequence of enrichment during subduction and subsequent metasomatism, craton margins become sites of metallogenesis (e.g., Mole et al., 2015). The western Kaapvaal craton margin (Figure 1a) also was affected by multiple episodes of accretion and collision in the Paleoproterozoic and Mesoproterozoic (Jacobs et al., 2008), and was intruded by two generations of xenolith-bearing magmas, lamproites in the Jurassic and kimberlites in the Cretaceous (Becker & Le Roex, 2006).

Eclogite xenoliths from the Prieska domain, at the southwestern Kaapvaal craton margin, at first glance are similar to those found in on-craton kimberlites, with coarse grain size and sub-equal proportions of garnet and omphacite-rich clinopyroxene (Tinguely et al., 2008). However, using detailed petrography as well as mineral composition and isotopic data, le Roex et al. (2020) showed that these samples are distinct in having equilibrated at considerably lower pressures than on-craton eclogite xenoliths, and rather derive from near the circum-cratonic crust-mantle boundary where mafic granulite converts to compositionally similar eclogite (Figure 1b). Emphasizing their kinship with craton-margin granulite xenoliths, the authors show that the eclogites' protoliths originated as basalts and plagioclase-rich cumulates that were transposed to greater depth during orogenesis and thickening during formation of the Namaqua-Natal Fold Belt (NNFB). As such, these samples offer the unique opportunity to investigate a range of processes associated with deep crust formation in collisional settings, and its physical state at the time of kimberlite magmatism.

The study of le Roex et al. (2020) focused on establishing the link between eclogite and granulite xenoliths from the Kaapvaal craton margin and provided a detailed analysis of the depths from which these samples were derived, within the context of the Namaqua-Natal orogeny. The present study aims at further deciphering the eclogites' chemical and redox evolution as part of the circumcratonic crust-mantle transition zone at the Kaapvaal craton margin. Toward this end, we obtained additional trace element data for the rock-forming minerals and $^{87}Sr/^{86}Sr$ for clinopyroxene, as well as $Fe^{3+}/\Sigma Fe$ in garnet in representative samples. This was combined with eclogite oxybarometry to obtain the first oxygen fugacity estimates for the crust-mantle transition zone in collisional orogens, which is a pivotal environment that modulates mass exchange between Earth's major reservoirs.

2. Geology, Prior Work, Samples, Petrography and Classification

The Kaapvaal craton consists of two distinct Archean nuclei, the Witwatersrand Block in the east and the Kimberley Block in the West, which underwent collision and stabilization some 2.9 Ga ago (Schmitz & Bowring, 2003). The western and southwestern craton margin was affected by Paleoproterozoic accretion and addition of the Kheis-Okwa-Magondi Belt, followed by 1.2–1.0 Ga collision with Paleoproterozoic microcontinents or arcs, high-grade metamorphism, granitoid formation and indentation-escape tectonics in the course of the Namaqua-Natal orogeny (Jacobs et al., 2008). The high-grade metamorphic NNFB formed largely during ca. 1.2–1.0 Ga orogenesis, but it remains unclear to which extent the basement in particular of the Namaqua sector is composed of older, Paleoproterozoic rocks (Jacobs et al., 2008). This uncertainty stems from the fact that much of the southern part of the NNFB consists of unexposed basement, which is covered by sediments and intrusive rocks of the Phanerozoic Karoo Supergroup. Apart from the cratonic Kimberley block, the Kheis belt, which includes reworked Archean basement, contains the most proximal exposed crust to the area of interest, which is located between the Namaqua and the Natal sectors, in the area of main convergence according to Jacobs et al. (2008) (Figure 1a). At up to ~45–55 km, the present-day seismic crustal thickness beneath the NNFB exceeds that of the Kaapvaal craton (35–40 km) (Nguuri et al., 2001) and may be related to severe collisional shortening and magmatic thickening during orogenesis (Schmitz & Bowring, 2003).

Both the Kaapvaal craton and the NNFB were intruded by Jurassic and Cretaceous lamproites and kimberlites (Becker & Le Roex, 2006), which are accordingly referred to as on-cratonic and circum- or off-cratonic (but see Pearson et al., 2021 for a new definition of cratons that encompasses post-Archean rocks), and which entrained mantle and crustal xenoliths that have been the subject of numerous studies (le Roex et al., 2020, and references therein). A comprehensive sample suite of predominantly bimineralic eclogites ± kyanite, plus garnet websterites and clinopyroxenites as well as mafic granulites, was previously investigated in detail by Tinguely et al. (2008) and le Roex et al. (2020). The host rocks are Cretaceous kimberlites (Jachtfontein, Lovedale, Roodekraal) from the Britstown area (le Roex et al., 2020) that were emplaced into the Prieska domain near the southwestern Kaapvaal craton margin. An exception is Markt, which is a lamproite northwest of Britstown with an

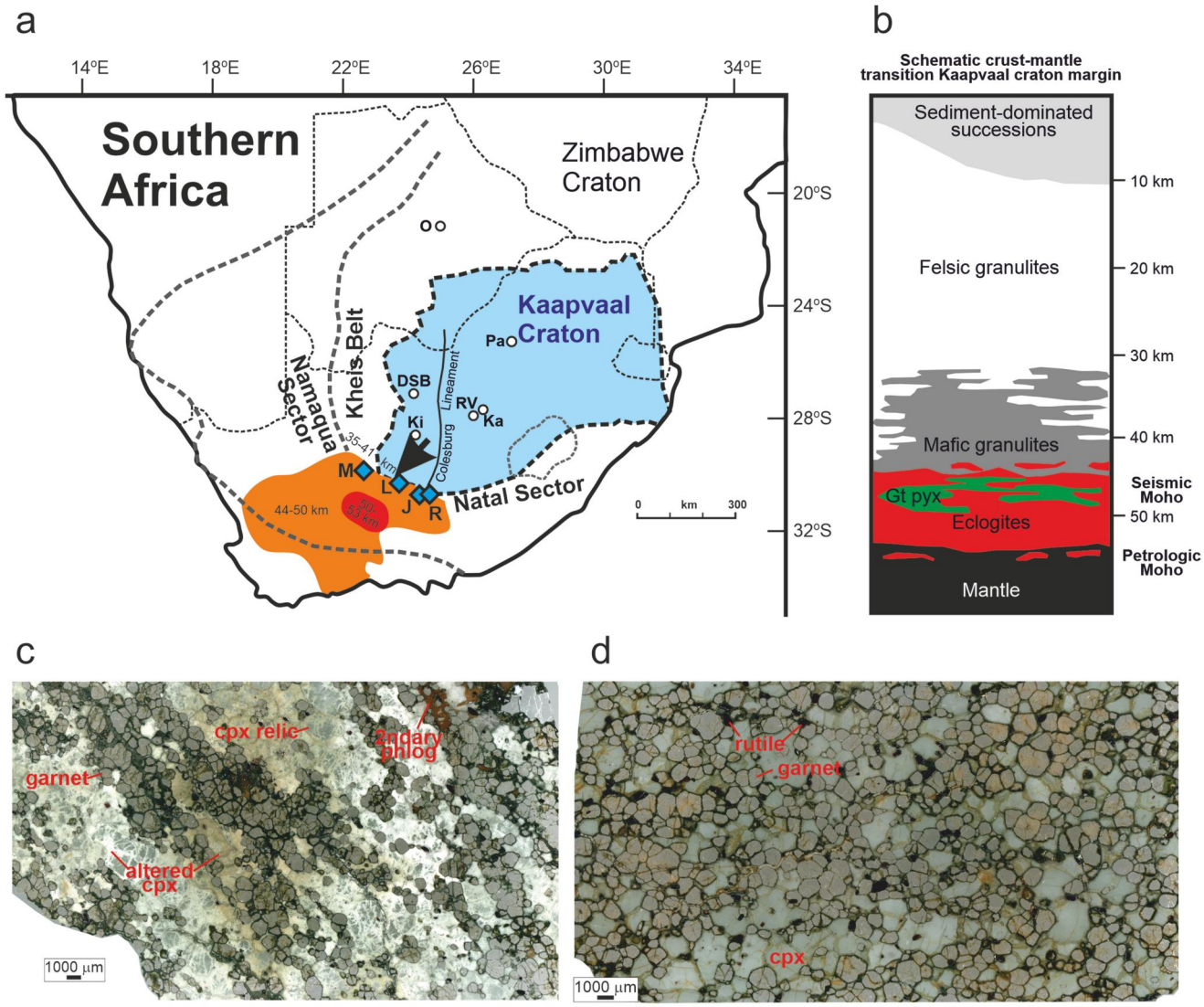

Figure 1. Map and schematic profile of the study area, as well as thin section images illustrating petrographic characteristics. (a) Outline of the Kaapvaal craton, adjoining Zimbabwe craton and Proterozoic mobile belts (Kheis, Namaqua-Natal) as well as approximate political boundaries (with thin stippled lines) (after le Roex et al. (2020), references therein). Blue diamonds denote kimberlite/lamproite localities in the study area at the southwestern Kaapvaal craton margin, comprising Markt (M), Lovedale (L), Jachtfontein (J) and Roodekraal (R); white circles denote other kimberlite/lamproite localities, including Orapa (O), Doornkloof-Sover-Bellsbank (DSB), Kimberley (Ki), Kaalvallei (Ka), Roberts Victor (RV), and Palmietfontein (Pa). Orange field and red field contained therein encircle crust with seismic thickness of 44–50 km and 50–53 km, respectively (from Nguuri et al. (2001)). (b) Schematic profile through the crust and crust mantle transition containing various lithologies (after le Roex et al. (2020)), with a petrologic Moho defined by transition to olivine-dominated rocks, which may be located at a different depth from the seismic Moho (O'Reilly & Griffin, 2013). (c) Eclogite 20263 from Jagersfontein showing strong banding of garnet (light pink) and clinopyroxene (cpx, alteration appearing white or greenish, pale greyish unaltered relics), plus secondary phlogopite (phlog), and foliation defined by the elongated arrangement of garnet clusters and shape-preferred orientation of clinopyroxene. (d) Eclogite JJG4541 from Roodekraal showing more evenly distributed garnet and clinopyroxene with interlocking fabric and mild foliation. Garnet alteration to kelyphite appears as thin dark rims. Rutile (black) is abundant.

emplacement age of 116 Ma (Smith et al., 1994). The seismic Moho beneath the kimberlite localities is located at ~44–50 km (Nguuri et al., 2001). Note that the petrologic Moho (O'Reilly & Griffin, 2013) may be deeper than the seismic Moho beneath the Prieska domain (Figure 1b), reaching down to 50–55 km (le Roex et al., 2020).

Prior investigation showed that the eclogites have distinct REE patterns, ranging from flat HREE patterns with small LREE-depletion (type 1), patterns with an inflection point at Sm or Nd (type 2), samples with strong LREE- and HREE-depletion (type 3), and flat or concave-up LREE patterns (type 4) (le Roex et al., 2020). They are derived from the thickened lower crust of the NNFB that was metamorphosed, together with compositionally similar garnet granulites, during ca. 1.2–1.0 Ga collision of the NNFB with the Kaapvaal craton (le Roex

et al., 2020). This is supported by ca. 1.1 Ga ages obtained for the granulites (Schmitz & Bowring, 2003) and a ca. 0.9 Ga Sm-Nd age array for the eclogites (le Roex et al., 2020).

Here, the focus is on 16 bimineralic (clinopyroxene plus garnet) eclogites, plus three sanidine- and one orthopyroxene-bearing samples (photographs in Figures 1c and 1d and Figure S1). Accessory rutile is subrounded to subhedral and occurs in all but six of the samples. Sulphide is identified in three samples, and quartz plus apatite in one sample (02G30). The eclogites are medium- to coarse-grained with granoblastic to mosaic granoblastic textures. Foliation defined by aggregates of garnet and by shape-preferred orientation of clinopyroxene is common. Garnet is subhedral to anhedral and tends to be fresh with minor kelyphitisation, whereas clinopyroxene is mostly anhedral and more prone to alteration. In eclogite 026203L, clinopyroxene occurs both in an interlocking texture with garnet and as porphyroclasts with garnet exsolution lamellae. Several samples show distinct banding of garnet and clinopyroxene, with parallel shape-preferred orientation of clinopyroxene and arrangement of garnet bands (e.g., 20263). In eclogite 20163, garnet appears as bands or veins that crosscuts bands of clinopyroxene having a weak shape-preferred orientation. Sanidine in 026203N appears as anhedral but discrete grains, whereas in 10063 sanidine occurs as a "pool" filling clinopyroxene interstices and in JJG2294 sanidine appears both as discrete grains and as interstice-filling "pools."

A summary of salient mineralogical and compositional features of the eclogites, which form the basis of their classification into enriched and gabbroic varieties, is given in Table 1. The type 1 pattern is displayed only by a single sample from Roodekraal (42223), the type 3 pattern by two samples from Roodekraal and four samples from Jachtfontein (of which 20163 has a distinct REE pattern with a positive slope in the MREE and relatively flat LREE and HREE, but similar strong Sr-Nd-Pb anomalies), whereas all four samples from Markt, all seven samples from Lovedale and another two from Roodekraal have the type 2 pattern (Figures 2a and 2b). The peculiar REE pattern of 20163 is recognizable in both clinopyroxene and garnet and therefore is a feature of the metamorphic rock (see mineral REE patterns in Figure S2 of the Supporting Information S1). The type 3 eclogites, the single type 1 eclogite and the single type 4 eclogite are all characterized by positive Eu, Sr, and Pb anomalies (Figures 2c and 2d), all of which point to plagioclase-rich cumulate protoliths (le Roex et al., 2020)—they will be collectively referred to hereafter as gabbroic in order to simplify. The remaining samples with higher LREE and MREE abundances will be referred to as enriched.

3. Sample Preparation, Analytical Techniques and Bulk Rock Reconstruction

All work in this study was carried out at Goethe-Universität Frankfurt. Rock pieces and cut-offs of variable sizes were available for study, of which three larger ones were made into thick sections (100 μm), and rock chips of the remainder were embedded in resin. Samples were polished in preparation for in situ analysis. A RESOlution (Resonetics) 193 nm ArF Excimer Laser, operated at 8 Hz and employing a spot size of 73 μm, with an on-sample fluence of ∼5 J.cm^{-2}, was linked to a Thermo Scientific ELEMENT XR inductively coupled plasma mass spectrometer (ICPMS) for determination of trace element abundances in garnet and clinopyroxene. Oxide production rate was tuned to ≤0.5% using ThO/Th. Quantification was achieved using reference glass NIST SRM 612 for sensitivity calibration and Si, previously determined by electron probe microanalyser (le Roex et al., 2020; Tinguely et al., 2008), as an internal standard. Several spots per grain and several grains per mineral were analyzed to assess homogeneity at the grain and sample scale. Data were reduced with the Glitter program (Griffin et al., 2008), using Ba as an indicator for accidental co-ablation of kimberlite material (e.g., in optically invisible minute cracks) in garnet and clinopyroxene, conservatively using 0.1 μg/g in garnet and 0.5 μg/g in clinopyroxene as an upper limit. The spectrum of each element was scrutinized for spurious peaks or signs of co-ablation of other phases. Individual analyses with measurement statistics are shown in Table S1. We use this complete, isogenous data set for the purpose of discussion and in plots. Basalt glass BIR-1G was analyzed repeatedly as an unknown ($n = 20$), and repeatability for most elements is well within 10% (Be, Rb, Ag, Cd, Ta, Bi, Th within 25%), while accuracy is within 19% except In (−30%) and Sn (−70%), based on GeoReM accepted values (http://georem.mpch-mainz.gwdg.de).

Strontium isotope ratios ($^{87}Sr/^{86}Sr$) were determined during two analytical campaigns using the same laser instrument but linked to a Thermo Scientific NEPTUNE PLUS multi-collector (MC) ICPMS, using Faraday Cups operated in static collection mode, spot size of 128 μm, 10 Hz repetition rate and an energy on the sample of 5–6 J cm^{-1}. The measurement routine included data acquisition for 45 s with 1 s integration time, and a gas blank was measured before sample ablation. Pre-ablation was not applied. Full details on the collector set-up and

Table 1
Summary of Petrographic and Compositional Features of Deep Crustal Eclogite Xenoliths From the Kaapvaal Craton Margin

Sample	Locality	REE type[a]	Group[b]	Cpx%[c]	Gt%[c]	Rt%[c]	Other acc%[c]	T °C[d]	P (GPa)[d]
02/1	Lovedale	2	Enriched, rt-free	45	55	0		1000	2.1
02100	Lovedale	2	Enriched, rt-free	55	45	0		899	1.7
02500	Lovedale	2	Enriched	58	39	3		895	1.6
026203L	Lovedale	2	Enriched	59	39	2	Snd	942	1.8
026203N	Lovedale	2	Enriched, snd-bearing	59	40	1	(<1)	990	2.0
02200	Lovedale	2	Enriched, rt-free	45	55	0		913	1.7
02G30	Lovedale	2	Enriched, rt-free	50	50	0	Qz, ap	923	1.7
10053	Markt	2	Enriched, rt-free	59	41	0		976	2.0
10063	Markt	2	Enriched, snd-bearing	48	44	3	Snd (5)	815	1.3
10093	Markt	2	Enriched	58	40	2		830	1.3
JJG2294	Markt	2	Enriched, snd-bearing	47	45	3	Snd (5)	885	1.6
42233	Roodekraal	2	Enriched, rt-free	54	46	0	Sf	915	1.7
42103	Roodekraal	2	Enriched, opx-bearing	41	19	3	Opx (37)	835	1.4
42143	Roodekraal	3	Gabbroic	50	47	3		870	1.5
42223	Roodekraal	1	Gabbroic, flat REE	42	56	2		858	1.5
JJG4541	Roodekraal	3	Gabbroic	50	47	3		860	1.5
20253	Jachtfontein	3	Gabbroic	49	50	1		830	1.3
20700	Jachtfontein	3	Gabbroic	49	49	2	Sf	871	1.5
20163	Jachtfontein	4	Gabbroic, MREE-depl.	59	39	2	Sf	851	1.4
20263	Jachtfontein	3	Gabbroic	44	54	2		865	1.5

Sample	$\delta^{18}O$ cpx[e]	$^{87}Sr/^{86}Sr$ cpx_{meas}[f]	$Fe^{3+}/\Sigma Fe$ gt[g]	ΔFMQ[h]	$\sigma \pm$[h]	$Fe^{3+}/\Sigma Fe$ cpx[i]	1σ	$Fe^{3+}/\Sigma Fe$ WR[i]	1σ
02/1	*5.3	0.70383	0.04	−0.9	0.5/0.6	0.29	0.08	0.08	0.02
02100	6.1	0.70399							
02500	7.4	0.70533	0.04	−1.2	0.6/0.8	0.24	0.07	0.07	0.02
026203L	6.6	0.70536							
026203N	*6.5	0.70342							
02200	5.3	0.70369	0.02	−1.7	0.9/1.5	0.17	0.04	0.04	0.01
02G30		0.70342	0.01	−1.7	0.7/1.0	0.06	0.02	0.01	0.01
10053	*6.8	0.70351							
10063		0.70405	0.03	−1.3	0.7/0.8	0.28	0.08	0.09	0.02
10093	5.8	0.70440							
JJG2294		0.70408	0.02	−2.3	0.9/1.4	0.20	0.06	0.06	0.01
42143	5.4	0.70336	0.02	−1.3	0.9/1.6	0.12	0.03	0.03	0.01
42233	6.1	0.70378	0.03	−1.4	0.7/0.8	0.40	0.10	0.10	0.02
42223	6.5	0.70347	0.02	−2.3	0.8/1.2	0.33	0.08	0.07	0.02
42103		0.70393	0.03	−0.9	0.8/1.0	0.28	0.07	0.06	0.01
JJG4541		0.70320	0.03	−3.1	0.8/1.1	0.22	0.06	0.06	0.01
20253	6.6	0.70344	0.02	−1.0	0.9/1.4	0.15	0.04	0.04	0.01
20700		0.70361	0.03	−0.5	0.6/0.8	0.29	0.08	0.07	0.01

Table 1
Continued

Sample	$\delta^{18}O$ cpx[e]	$^{87}Sr/^{86}Sr$ cpx_{meas}[f]	$Fe^{3+}/\Sigma Fe$ gt[g]	ΔFMQ[h]	$\sigma \pm$[h]	$Fe^{3+}/\Sigma Fe$ cpx[i]	1σ	$Fe^{3+}/\Sigma Fe$ WR[i]	1σ
20163		0.70288	0.02	−1.6	0.7/1.0	0.23	0.06	0.05	0.01
20263		0.70332	0.04	−1.2	0.5/0.6	0.25	0.07	0.07	0.01

Note. opx orthopyroxene, cpx clinopyroxene, gt garnet, rt rutile, acc accessory (primary assemblage only), qz quartz, ap apatite, snd sanidine, sf sulphide. [a]REE pattern according to le Roex et al. (2020): 1 flat HREE, small LREE-depletion, 2 inflection point at Sm or Nd, 3 strong LREE- and HREE-depletion, 4 flat or concave-up HREE. [b]Enriched = LREE-enriched; gabbroic = positive Eu-anomalies indicative of a plagioclase-rich protolith. [c]Mineral modes and temperatures of last equilibration from Tinguely et al. (2008) and le Roex et al. (2020); Cpx, Gt, Rt and numbers given in parentheses for other minerals refer to volume% of the mineral in the rock; 0 vol% in rutile indicates that rutile has not been observed in either prior or this work. [d]Temperature and pressure were calculated by assuming a linear relationship with the temperature extremes of 815 and 1000°C within the pressure interval of 1.7 ± 0.4 GPa given in le Roex et al. (2020). [e]$\delta^{18}O$ is the deviation of $^{18}O/^{16}O$ expressed in parts per thousand relative to that of VSMOW given in le Roex et al. (2020), except those marked with *: in order to increase the number of observations and since measured $\delta^{18}O$ in garnet and cpx are strongly correlated ($r^2 = 0.84$ for $n = 7$), we calculate $\delta^{18}O$ in clinopyroxene from that in garnet and vice versa for samples where corresponding data for garnet are unavailable, using the regression derived from the data set in le Roex et al. (2020): garnet $\delta^{18}O = 0.6679 \times$ cpx $\delta^{18}O + 1.7305$. [f]Measured (meas) ratios; the less radiogenic value is given for 02G30 and 026203N where two isotopic populations are identified (Table S2 in Supporting Information S1). [g]The full data set for $Fe^{3+}/\Sigma Fe$ in garnet and associated major- and minor-element compositions is reported in Table S3 of the Supporting Information S1. [h]Oxygen fugacity relative to the fayalite-magnetite-quartz oxygen buffer is expressed as $\Delta \log f_{O2}$ (FMQ) and calculated using the oxybarometer of Stagno et al. (2015); uncertainty, which is asymmetric, is estimated by propagating the absolute measurement uncertainty on garnet $Fe^{3+}/\Sigma Fe$ (±0.01) and pressure-temperature along a conductive geotherm (±60°C, ±0.4 GPa, respectively; see Aulbach et al., 2022, for more details). [i]$Fe^{3+}/\Sigma Fe$ in clinopyroxene was calculated using the measured $Fe^{3+}/\Sigma Fe$ in garnet and the distribution D of V between clinopyroxene and garnet, which are related according to the equation $(cpx/gt D(Fe^{3+}/\Sigma Fe) = 1.67 \pm 0.37 \times cpx/gt D(V) + 1.45 \pm 0.71$ (1σ); Aulbach et al., 2022); corresponding 1σ are propagated from uncertainty in slope and intercept of the relationship; bulk rock $Fe^{3+}/\Sigma Fe$ is reconstructed from that of clinopyroxene and garnet using modal abundances given in this table, weighted by their Fe contribution; corresponding 1σ are propagated from the uncertainties on garnet and clinopyroxene $Fe^{3+}/\Sigma Fe$ and an assumed total uncertainty on modal abundances of 10% (see Aulbach et al., 2022, for more details).

interference corrections are reported in Aulbach et al. (2016). Several grains per sample with up to two spots per grain were analyzed, depending on the available material. In order to monitor instrument performance, two basalt glass reference materials and a plagioclase in-house standard with variable $^{87}Rb/^{86}Sr$ were analyzed repeatedly as unknowns. The reference materials BHVO-1 ($^{87}Rb/^{86}Sr = 0.065$) and BCR-2G ($^{87}Rb/^{86}Sr = 0.39$) require a large correction of the isobaric interference of ^{87}Rb on ^{87}Sr. Results for BHVO-1 are $^{87}Sr/^{86}Sr$ of 0.70332 ± 0.00021 (1σ, $n = 6$) and 0.703436 ± 0.000040 ($n = 5$), and for BCR-2G they are 0.70499 ± 0.00035 ($n = 6$) and 0.704891 ± 0.000047 ($n = 5$), respectively, for two analytical campaigns. These values are indistinguishable from or close to GeoReM-preferred values of 0.703469 ± 0.000007 and 0.705003 ± 0.000004, respectively (http://georem.mpch-mainz.gwdg.de). The in-house plagioclase standard (MIR-1) with $^{87}Rb/^{86}Sr$ (0.0031) similar to clinopyroxene in this study (0.0015) gave 0.703071 ± 0.000073 (1σ, $n = 6$) and 0.703078 ± 0.000011 ($n = 5$) compared to the Thermal Ionization Mass Spectrometry-derived values of 0.703096 ± 0.000050 (Table S2 in Supporting Information S1).

Bulk rocks are reconstructed with measured mineral modes reported in le Roex et al. (2020), determined by counting >1,000 points on thin sections. Rutile was treated as pure TiO_2, using modal volumes, a rutile density of 4.25 $g.cm^{-3}$ and average density of the eclogitic silicate assemblage of 3.60 $g.cm^{-3}$ (Aulbach, Massuyeau, et al., 2020). Given the affinity of Zr, Hf, Nb, Ta, and U for rutile (e.g., Klemme et al., 2005), the abundances of these elements in bulk rocks reconstructed without rutile are minima.

A representative set comprising 15 samples was chosen for determination of $Fe^{3+}/\Sigma Fe$ by the "Flank Method" in garnet, which employs the intensity ratio variations of the Fe Lα and Fe Lβ X-ray emission lines together with a correction for Fe self-absorption (Höfer & Brey, 2007). The in situ Flank Method, which has since been adopted by many laboratories (e.g., Malaspina et al., 2009, 2017; Tang et al., 2019; Tao et al., 2018), yields data comparable to those derived from the more widely known Mössbauer technique (Höfer & Brey, 2007), and to electron energy-loss spectroscopy (Malaspina et al., 2010) and micro-X-Ray absorption near-edge structure microscopy (Borfecchia et al., 2012). Importantly, it allows assessment of homogeneity of the samples—a conclusion not afforded by bulk Mössbauer analyses. In contrast to the original study by Höfer and Brey (2007), the JEOL JXA-8530F Plus Hyper Probe was used here, which allows the simultaneous determination of $Fe^{3+}/\Sigma Fe$ using large TAP analyzer crystals in two different spectrometers (2TAPL and 4TAPL) at significantly enhanced count rates. A series of four natural garnet standards described in McGuire et al. (1992: Almandine H112140), Rankenburg et al. (2004: Damknolle), Creighton (2009: UA5 and unpublished: UA17), for which $Fe^{3+}/\Sigma Fe$ has been independently determined via wet chemical analysis and/or Mössbauer spectroscopy, are used for calibration together with further secondary standards for quality control (more details on the standards in Table

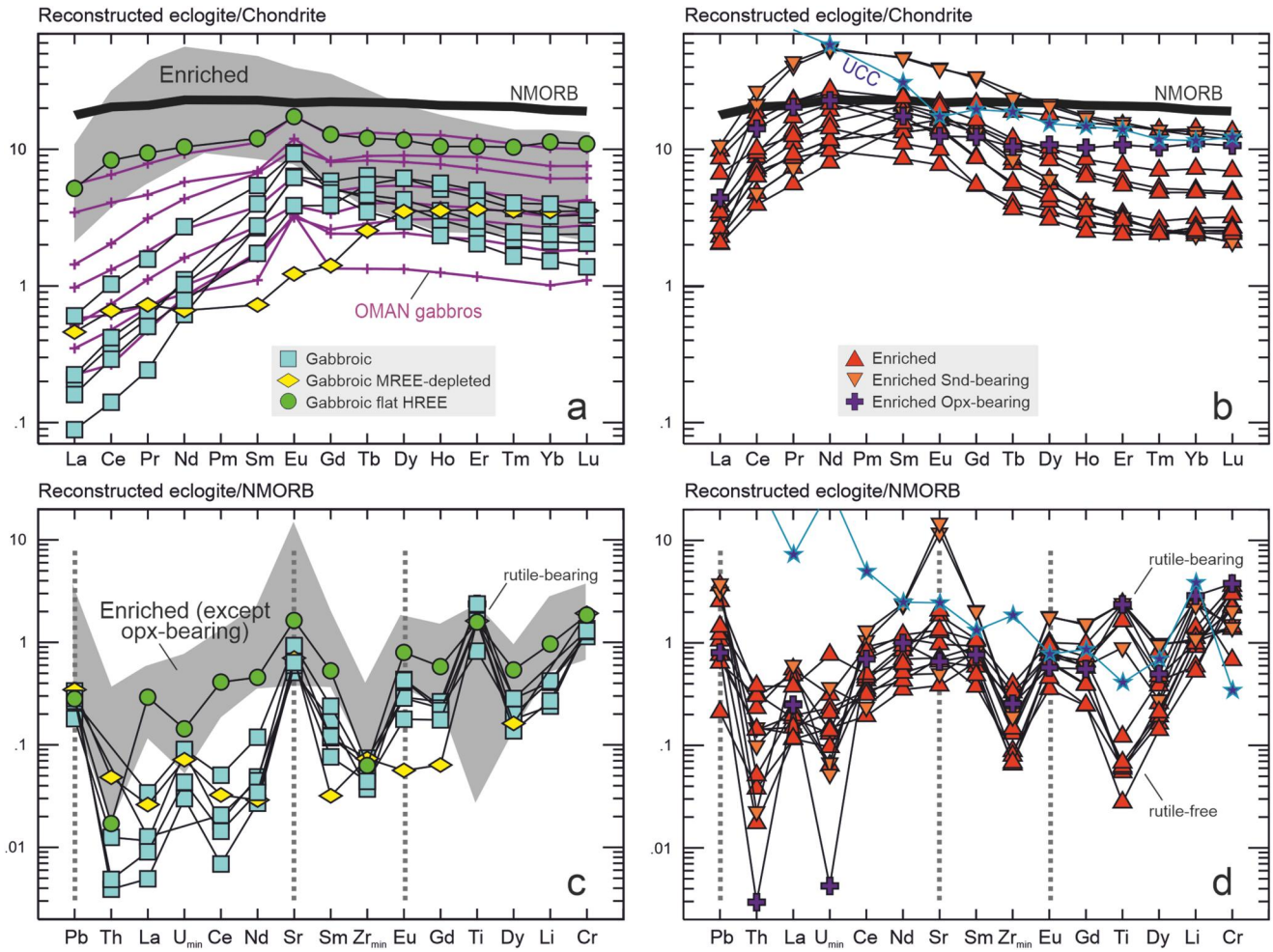

Figure 2. Trace element patterns of reconstructed bulk eclogite xenoliths from the Kaapvaal craton margin. (a, b) Chondrite-normalized REE patterns and (c, d) NMORB-normalized extended trace element patterns. For clarity, enriched eclogites (Table 1) comprising one orthopyroxene-bearing and three sanidine-bearing samples are shown separately from gabbroic eclogites with marked positive Eu-anomalies, including one sample with distinctly flat HREE-pattern and one sample with a peculiar MREE-depleted pattern. Enriched samples are shown as gray fields in (a) and (c) to illustrate differences. Shown for comparison are NMORB from Gale et al. (2013), upper continental crust (UCC) from Rudnick and Gao (2014) and a variety of gabbros and troctolites from the Oman ophiolite (Benoit et al., 1996). Chondrite of McDonough and Sun (1995), NMORB of Gale et al. (2013). Abundances of Zr and U are minima since rutile was not considered in reconstruction.

S3 of the Supporting Information S1). Analyses were carried out in two different locations in two garnet grains per sample by measuring 25 spots in a grid in each location, corresponding to a total of 50 $Fe^{3+}/\Sigma Fe$ determinations and 25 major- and minor-element compositions in each garnet grain (Table S3 in Supporting Information S1). The uncertainty in $Fe^{3+}/\Sigma Fe$ determination depends on Fe concentration and for the instrument used is between ±0.01 and 0.02 1σ for peridotitic garnet with generally <<10 wt.% FeO content (Woodland et al., 2021). As eclogitic garnet in this study contains 16.5 wt.% FeO on average, the $Fe^{3+}/\Sigma Fe$ uncertainty is closer to ±0.01 (Figure S3 in Supporting Information S1).

4. Results

4.1. Trace Elements in Minerals and Reconstructed Whole Rocks

As the abundances of many trace elements have been reported previously (le Roex et al., 2020), the following description focuses on those not previously determined (Li, Be, Co, Cu, Zn, Ga, Ag, Cd, In, Sn, Lu, Bi). Compared to gabbroic eclogites, clinopyroxene in 12 enriched samples, excluding the orthopyroxene-bearing eclogite (R42103), tends to have higher median trace-element abundances of Li (12.5 vs. 4.7 μg/g), Be (0.78 vs. 0.48 μg/g), Zn (73 vs. 51 μg/g), Sn (0.62 vs. 0.17 μg/g) and Bi (0.006 vs. 0.003 μg/g) (some elements listed in

Table 2
Some Geochemical Characteristics Distinguishing Reconstructed Bulk Gabbroic and Enriched Deep Crustal Eclogite Xenoliths From the Kaapvaal Craton Margin (Oxides in wt.%, Trace Elements in μg/g)

Sample	Er/Lu_{NMORB}	Nb/Yb_{NMORB}	Eu/Eu*	Sr	Pb	SiO_2	TiO_2	Al_2O_3	MgO	Na_2O	Li
Gabbroic eclogites ($n = 5$)[b]											
42143	1.16	0.44	2.05	4.5	7.9	46.4	3.6	15.4	10.4	2.0	1.46
JJG4541	1.22	0.27	1.60	11.2	11.0	45.7	3.6	15.4	9.6	2.2	2.49
20253	1.14	0.22	1.66	8.1	35.9	47.6	1.3	15.9	12.7	1.8	2.56
20700	1.35	1.51	1.81	5.2	4.2	46.0	2.5	16.7	11.2	2.2	1.64
20263	1.27	0.17	1.49	11.5	14.8	45.7	2.5	16.9	9.6	1.9	na
Minimum	1.14	0.17	1.49	4.5	4.2	45.7	1.3	15.4	9.6	1.8	1.46
Maximum	1.35	1.51	2.05	11.5	35.9	47.6	3.6	16.9	12.7	2.2	2.56
Average	1.23	0.52	1.72	8.1	14.8	46.3	2.7	16.1	10.7	2.0	2.03
1σ	0.08	0.56	0.22	3.2	12.5	0.8	1.0	0.7	1.3	0.2	0.57
Median	**1.22**	**0.27**	**1.66**	**8.1**	**11.0**	**46.0**	**2.5**	**15.9**	**10.4**	**2.0**	**2.06**
Enriched eclogites ($n = 12$)[c]											
02/1[a]	1.11	1.34	1.11	0.8	0.9	47.0	0.2	18.0	10.4	2.7	3.59
02100[a]	0.97	6.86	1.11	0.9	1.1	48.4	0.1	16.2	12.8	2.2	8.59
02200[a]	0.98	3.24	1.13	1.8	2.0	47.0	0.1	17.5	12.7	1.7	5.56
02G30[a]	0.90	3.67	1.32	1.2	2.0	48.5	0.1	18.1	11.8	2.6	6.87
10053[a]	1.15	7.46	1.20	1.6	1.9	48.8	0.1	17.3	11.8	2.8	6.80
42233[a]	0.85	4.75	1.27	3.7	2.6	48.2	0.0	14.1	14.4	1.9	3.20
02500	1.01	1.16	0.95	1.9	6.7	47.2	3.7	13.5	9.6	2.8	16.05
026203L	1.05	2.77	0.97	0.9	5.7	47.5	2.5	14.0	9.8	2.8	15.28
10093	1.01	3.20	1.03	1.2	0.7	47.1	2.5	12.2	12.0	1.8	6.04
026203N	1.38	4.02	1.03	0.8	2.4	48.2	1.4	16.5	8.9	3.4	14.19
10063	1.15	3.37	1.03	1.4	2.1	45.8	3.7	13.8	9.0	1.7	6.25
JJG2294	1.17	3.67	0.97	6.6	2.2	45.7	3.7	13.7	8.6	1.8	6.67
Minimum	0.85	1.16	0.95	0.76	0.68	45.67	0.04	12.2	8.6	1.7	3.2
Maximum	1.38	7.46	1.32	6.63	6.73	48.80	3.70	18.1	14.4	3.4	16.0
Average	1.06	3.79	1.09	1.90	2.53	47.46	1.50	15.4	11.0	2.3	8.3
1σ	0.14	1.87	0.12	1.70	1.84	1.03	1.60	2.1	1.9	0.6	4.4
Median	**1.03**	**3.52**	**1.07**	**1.3**	**2.1**	**47.3**	**0.8**	**15.1**	**11.1**	**2.4**	**6.73**

Sample	Be	Cr	Ni	Cu_{min}	Zn	Sr	Y	Zr_{min}	Pb	Th	U
Gabbroic eclogites ($n = 5$)[b]											
42143	0.086	357	118	0.86	57	65	4.2	3.8	0.092	0.0032	0.0070
JJG4541	0.334	300	94	1.07	61	116	7.1	7.6	0.146	na	na
20253	0.224	335	83	0.38	50	76	4.7	6.1	0.171	0.0010	0.0025
J0700	0.104	356	90	0.55	44	119	3.1	5.5	0.136	na	0.007
20263	na	342	38	na	54	81	7.7	4.5	0.145	0.0012	0.0036
Minimum	0.086	300	38	0.38	44	65	3.1	3.8	0.092	0.0010	0.0025
Maximum	0.334	357	118	1.07	61	119	7.7	7.6	0.171	0.0032	0.0075
Average	0.187	338	85	0.72	53	91	5.4	5.5	0.138	0.0018	0.0051
1σ	0.116	24	29	0.31	7	24	1.9	1.5	0.029	0.0012	0.0025
Median	**0.164**	**342**	**90**	**0.71**	**54**	**81**	**4.7**	**5.5**	**0.145**	**0.0012**	**0.0053**

Table 2
Continued

Sample	Be	Cr	Ni	Cu_{min}	Zn	Sr	Y	Zr_{min}	Pb	Th	U
Enriched eclogites (n = 12)[c]											
02/1[a]	0.627	606	61	0.56	80	49	10.4	28.9	0.107	0.0095	0.0122
02100[a]	0.330	947	348	1.47	62	124	5.8	13.3	0.537	0.0582	0.0259
02200[a]	0.210	850	349	5.64	54	91	4.3	9.0	0.389	0.0357	0.0192
02G30[a]	0.264	377	265	2.84	68	84	4.5	6.6	0.389	0.0361	0.0172
10053[a]	0.321	849	326	1.83	53	163	4.8	8.1	0.622	0.0044	0.0080
42233[a]	0.236	784	238	0.37	33	265	3.7	6.9	0.733	0.0956	0.0635
02500	1.242	359	95	0.59	148	237	22.8	40.2	1.860	0.0128	0.0053
026203L	1.212	178	86	1.64	128	91	9.4	33.4	1.301	0.0803	0.0108
10093	0.239	582	45	0.25	88	171	11.9	14.8	0.327	0.0764	0.0115
026203N	0.912	396	103	0.75	99	64	6.2	18.2	0.355	0.0374	0.0305
10063	0.468	372	177	0.31	158	1,512	24.6	21.1	1.592	0.0250	0.0056
JJG2294	0.521	538	na	0.34	156	1,884	23.9	19.4	1.922	0.0057	0.0043
Minimum	0.21	178	45	0.25	33	49	3.7	6.6	0.11	0.004	0.004
Maximum	1.24	947	349	5.64	158	1,884	24.6	40.2	1.92	0.096	0.063
Average	0.55	570	190	1.38	94	395	11.0	18.3	0.84	0.040	0.018
1σ	0.38	243	119	1.56	44	617	8.1	11.0	0.65	0.031	0.017
Median	**0.399**	**560**	**177**	**0.67**	**84**	**143**	**7.8**	**16.5**	**0.579**	**0.0359**	**0.0119**

Note. Subscript NMORB denotes normalization to values from Gale et al. (2013); Eu/Eu* is chondrite-normalized Eu/(Sm*Gd)^0.5 (chondrite of McDonough and Sun (1995)), Sr* is NMORB-normalized Sr/(0.5*Nd + 0.5*Sm) and Pb* is NMORB-normalized Pb/(0.5*Ce + 0.5*Pr); whole rocks reconstructed from mineral compositions weighted by modes given in Table 1, values are only calculated if above the detection limit in both garnet and clinopyroxene; Cu and Zr abundances are minima because sulphide and rutile, respectively, were not considered in reconstruction. The median values are given in bold font to facilitate comparison amongst the two groups. [a]Rutile-free eclogites. [b]Does not include sample 42223 with distinct, flat HREE pattern and sample J20163 with peculiar MREE depletion. [c]Does not include sample 42103 containing 37 vol.% orthopyroxene.

Table 2, all data in Table S1). In contrast, Cu (1.1 and 1.0 μg/g), Ga (11.3 and 10.8 μg/g), Ag (0.048 and 0.052 μg/g), Cd (0.072 and 0.057 μg/g) and In (0.033 and 0.037 μg/g) abundances are more similar in the two groups. With the exception of higher Li (27.8 μg/g), Cd (0.28 μg/g), and lower Cu (0.33 μg/g), trace-element abundances in clinopyroxene from orthopyroxene-bearing eclogite 42103 fall within the range of enriched eclogites. Clinopyroxene in gabbroic eclogite 20163 with the unusual MREE-depleted pattern (Figure 2a) has abundances of other trace elements largely within the range of other gabbroic eclogites. In contrast, clinopyroxene in gabbroic eclogite 42223, which has higher REE abundances and a flatter REE pattern than the other gabbroic eclogites (Figure 2a), also features higher contents of other trace elements, such as Li (13.2 μg/g), Be (0.94 μg/g), Zn (89 μg/g), Cd (0.143 μg/g), In (0.076 μg/g), and Sn (0.96 μg/g).

Similar systematics to those in clinopyroxene are observed in garnet from enriched versus gabbroic eclogites, with 0.86 versus 0.22 μg/g Li, 93 versus 58 μg/g Zn, 3.2 versus 2.7 μg/g Ga, and 0.058 versus 0.034 μg/g Sn (some elements listed in Table 2). A garnet inclusion in clinopyroxene from sample JJG4541 has very similar concentrations to matrix garnet. Garnet in orthopyroxene-eclogite 42103 again has higher Li (2.0 μg/g) and Cd (0.31 μg/g) concentrations. Orthopyroxene in this sample is heterogeneous with respect to Ti, Zr, and Hf contents (Table S1). It has appreciable abundances of Li (15.7 μg/g), Ni (1,090 μg/g), and Zn (400 μg/g), but lower abundances of other elements than garnet and clinopyroxene. Barium is present as a structural component in sanidine in three eclogites (026203N, 10063, JJG2294), with BaO concentrations of 2.5–5.7 wt%. Sanidine contains <10 μg/g of Li, Sc, Cr, Cu, and Y, and 71–160 μg/g Zn. The isolated grain in 026203N is generally less enriched than sanidine occurring as pools in the other two samples, having 194 μg/g Sr (vs. >20,000 μg/g), 0.04 μg/g Ce (vs. >0.39 μg/g), and 0.14 μg/g Pb (vs. >24 μg/g). Exceptions are 5.7 wt% BaO and 37 μg/g Rb in the isolated sanidine grain versus <3.7 wt% and <8.6 μg/g in sanidine from pools. Despite low oxide production

rates (Methods), extreme Ba concentrations in sanidine imply significant overlap of BaO on Eu and of doubly charged ^{138}Ba on ^{69}Ga, and concentrations for these elements are therefore not reported.

Median calculated bulk-rock abundances in enriched eclogites are ≥1.5 times higher than in gabbroic eclogites for Li, Be, Cr, Ni, Zn, Y, Zr_{min}, Nb_{min}, Sn, all REE, Hf_{min}, Ta_{min}, Pb, Bi, Th, and U, of which the LREE and Th show the greatest difference (>17 and 25 times, respectively) (some listed in Table 2). Conversely, gabbroic eclogites, including 42223, show extreme enrichment in Eu, Sr, and Pb relative to REE of similar compatibility during mantle melting, that is, Sm and Gd, Nd and Sm, and Ce and Pr, respectively (choice of elements follows the order of decreasing incompatibility during mantle melting of Hofmann (1997)). This is expressed as Eu/Eu* (chondrite-normalized Eu/(Sm*Gd)^0.5), Sr* (NMORB-normalized Sr/(0.5*Nd + 0.5*Sm)) and Pb* (NMORB-normalized Pb/(0.5*Ce + 0.5*Pr)). Median Eu/Eu*, Sr*, and Pb* in gabbroic eclogites are 1. 7, 8.1, and 10.9, respectively, compared to 1.1, 1.3, and 2.0 for enriched eclogites (Table 2).

4.2. Strontium Isotope Ratios in Clinopyroxene

Measured Sr isotope ratios ($^{87}Sr/^{86}Sr$) in clinopyroxene from all samples range from 0.70288 ± 0.00012 (2 standard errors, $n = 1$) to 0.70536 ± 0.00024 (1σ, $n = 5$), while $^{87}Rb/^{86}Sr$ ranges from 0.00001 ± 0.00001 (1σ, $n = 6$) to 0.00043 ± 0.00012 (1σ, $n = 3$) (Table S2 in Supporting Information S1). There is no co-variation of $^{87}Rb/^{86}Sr$ with $^{87}Sr/^{86}Sr$, and at the very low measured $^{87}Rb/^{86}Sr$, initial $^{87}Sr/^{86}Sr$ calculated for the time of eruption (117 Ma for Markt, 74 Ma for the other localities; Smith et al., 1994) and even at 1 Ga (~the end of the Namaqua-Natal orogeny; denoted as $^{87}Sr/^{86}Sr_{(1Ga)}$), are mostly insignificantly lower. The uncertainty for multiple Sr isotope measurements per sample (multiple spots per grain and/or multiple grains per sample) is 0.00013 ($n = 42$; 1σ), similar to the average measurement uncertainty (0.00016; 2 standard errors). Thus, the samples are homogeneous with respect to $^{87}Sr/^{86}Sr$, with the exception of clinopyroxene in sample 026203N, where one grain has $^{87}Sr/^{86}Sr$ of 0.70342 ± 0.00016 (1σ, $n = 3$), whereas two other grains have 0.70413 ± 0.00004 ($n = 2$), and 02G30, where one grain has $^{87}Sr/^{86}Sr$ of 0.70505 ± 0.00019 (2 standard errors, $n = 1$), whereas two other grains have 0.70342 ± 0.00024 ($n = 4$). For these two samples, the less radiogenic values are discussed and displayed. The average difference of the in situ $^{87}Sr/^{86}Sr$ acquired in this study, and the solution $^{87}Sr/^{86}Sr$ reported for clinopyroxene separates in le Roex et al. (2020) is 0.0005 (Table S2 in Supporting Information S1). This is larger than the analytical uncertainty and may reflect sample heterogeneity, as also detected in this study, and/or the inclusion in the separates of partially isotopically enriched rims, whereas the LAM method affords acquisition of data in the clear cores of clinopyroxene grains.

4.3. Oxidation State of Fe in Garnet, and Bulk $Fe^{3+}/\Sigma Fe$ and Oxygen Fugacity Estimates

Garnet $Fe^{3+}/\Sigma Fe$ is very low, ranging from 0.01 ± 0.01 to 0.04 ± 0.01 (Table 1). There is no systematic difference between enriched and gabbroic eclogites. Clinopyroxene $Fe^{3+}/\Sigma Fe$ is calculated using the empirical relationship for the distribution of Fe^{3+} between clinopyroxene and garnet, which is correlated with V distribution according to equation $D(Fe^{3+}/\Sigma Fe)_{cpx\text{-}grt} = 1.67\ (\pm 0.37) * D(V)_{cpx\text{-}grt} + 1.45\ (\pm 0.71\ 1\sigma)$, possibly because V has similar temperature, composition and redox sensitivity to Fe^{3+} (Aulbach et al., 2022). Estimates for clinopyroxene $Fe^{3+}/\Sigma Fe$ range from 0.06 ± 0.02 to 0.40 ± 0.10 (uncertainties reflect propagated uncertainties on the slope and intercept). Bulk-rock $Fe^{3+}/\Sigma Fe$ is then estimated using measured garnet and clinopyroxene modes (Table 1), weighted by their Fe contribution, and ranges from 0.01 ± 0.01 to 0.10 ± 0.02 (Table 1). Uncertainties are propagated from the uncertainties on garnet and clinopyroxene $Fe^{3+}/\Sigma Fe$, weighted by their Fe contribution (hence dominated by garnet with measured $Fe^{3+}/\Sigma Fe$ and correspondingly lower uncertainties), and an assumed total uncertainty on modal abundances of 10% (see Aulbach et al., 2022, for more details).

Pressure and temperature estimates given in Table 1 are employed for oxygen fugacity calculations, using the oxybarometer of Stagno et al. (2015), which is based on an equilibrium between eclogite minerals in the presence of free SiO_2 and does not require that $Fe^{3+}/\Sigma Fe$ of clinopyroxene be known. As emphasized in Aulbach et al. (2022), even when $Fe^{3+}/\Sigma Fe$ in garnet and clinopyroxene are known, input temperatures should be calculated using total Fe content in exchange thermometers, which yields more accurate results and reflects that most thermometers are calibrated on experiments containing some amount of ferric iron. Resultant oxygen fugacities relative to the Fayalite-Magnetite-Quartz buffer ($\Delta \log fO_2$(FMQ), hereafter FMQ) vary from −3.1 (±1.0) to −0.5 (±0.7; average of asymmetric uncertainties $\sigma+$ and $\sigma-$ is given) (Table 1). These uncertainties reflect the propagated uncertainties of ±0.01 on garnet $Fe^{3+}/\Sigma Fe$, of 60°C on temperature and of 0.4 GPa on pressure, the

latter corresponding to the standard deviation of all pressures calculated for the Prieska suite by Le Roex et al. (2020). Given that various approaches adopted by Le Roex et al. (2020) yield similar pressure-temperature results (Fe-Mg and REE exchange, pseudosection modeling), these adopted pressure-temperature uncertainties are considered to be realistic.

The number of Si cations per formula unit (cpfu) in clinopyroxene in these samples deviates from the ideal occupancy of 2 (1.981–1.986; e.g., reflecting Ca-Tschermaks component $CaAl_2SiO_6$), which may reflect some degree of silica-undersaturation. This would imply that the calculated fO_2 are maxima and have added uncertainties (Aulbach et al., 2017; Smart, Tappe, Woodland, Greyling, et al., 2021). Aluminous eclogite xenoliths, which are often kyanite- and sometimes corundum-bearing, tend to have lower Si cpfu than high-temperature eclogite xenoliths (Figure S4a in Supporting Information S1). Unfortunately, in the absence of corundum, the silica activity ($aSiO_2$) cannot be directly determined in the craton-margin eclogites, but it has been quantified to $aSiO_2 = 0.42$ in a corundum-bearing eclogite xenolith from the Kaapvaal craton (1.92 cpfu in clinopyroxene), resulting in an fO_2 overestimate by 1.5 orders of magnitude (Smart, Tappe, Woodland, Greyling, et al., 2021). On the other hand, sample 02G30 with 1.948 cpfu Si in clinopyroxene has been identified as quartz-bearing (Tinguely et al., 2008), so Si cpfu is not an accurate indicator of silica undersaturation. Nevertheless, there is a tendency for samples from the Kaapvaal craton with low clinopyroxene Si cpfu to have high fO_2 (Figure S4b in Supporting Information S1), and it is important to bear in mind that the fO_2 values in silica-undersaturated samples represent maxima.

5. Discussion

5.1. Deep Crustal Origin of Craton-Margin Eclogites and Their Prograde Metamorphic Evolution

Using a variety of approaches, le Roex et al. (2020) estimated pressures for the Kaapvaal craton margin eclogites at ~1.7 ± 0.4 GPa, and interpreted them as part of a collisionally thickened crust-mantle transition. It is notable that the CaO distribution between clinopyroxene and garnet decreases markedly with increasing temperature (for a fixed pressure of 1.5 GPa) in these samples, whereby enriched and gabbroic eclogites form sub-parallel trends reflecting bulk compositional differences (Figure 3a). This is accompanied by changes in jadeite component in clinopyroxene, which increases with temperature (Figure 3b). As the jadeite-forming reaction is strongly pressure- but weakly temperature-dependent (Kushiro, 1969), this apparent temperature-dependence suggests that the samples actually equilibrated over a discrete pressure interval along a geothermal gradient. Their relatively shallow origin, as part of a thickened crust-mantle transition, is supported by the occurrence of a composite granulite-eclogite xenolith in the suite (le Roex et al., 2020). It is further evident from the lower TiO_2 (or rutile solubility) and Na_2O in garnet, which are temperature-dependent along conductive geotherms (Aulbach, 2020), relative to on-craton mantle eclogites derived from greater pressures and temperatures (Figure 3c). A notable exception are amphibole-bearing eclogite xenoliths from Palmietfontein, the unusual low-temperature origin of which was noted (Smart, Tappe, Woodland, Harris, et al., 2021). Finally, compared to high-temperature on-craton eclogite xenoliths, incompatible trace elements (e.g., Ce) partition more strongly into clinopyroxene than into garnet at a given grossular content in craton-margin eclogites (Figure 3d), again reflecting low temperatures of equilibration with reduced partitioning into garnet (Aulbach, Massuyeau, et al., 2020).

Gabbroic eclogite xenoliths show all the hallmarks of a plagioclase-rich protolith (le Roex et al., 2020). They are generally incompatible-element poor (Table 2) and have low total REE contents that reflect their cumulate character, with generally strong exclusion of incompatible elements. Exceptions are Eu, Pb, and Sr, which are less incompatible in plagioclase than REE of similar incompatibility during mantle melting, and therefore produce strong positive anomalies (Figures 2a and 2c). These samples have REE patterns similar to gabbros and troctolites from the Oman ophiolite, which contains MORB-like crust (Benoit et al., 1996) (Figure 2a). Partial melt extraction is therefore not required to explain the LREE-depletion of gabbroic eclogites. Eclogite 20163 shares strong positive Pb and Sr anomalies (Table 2), and low temperature of last equilibration with gabbroic eclogites (Table 1), but it has a peculiarly MREE-depleted pattern (Figure 2a), which cannot be produced by igneous processes. This feature is typical of oceanic crust that interacted with a deserpentinization fluid, and has also been recognized in on-craton eclogite xenoliths (Aulbach, Viljoen, & Gerdes, 2020). Finally, clinopyroxene in two gabbroic eclogites (20253, 42223) displays $\delta^{18}O$ outside the canonical mantle range (5.5 ± 0.4‰; Mattey et al., 1994) (Table 1), which may reflect low-temperature seawater alteration (e.g., Jacob, 2004; Smart et al., 2014). Deep crustal NNFB eclogites thus potentially represent "missing" samples of one or multiple ocean basins that were closed during proposed terrane collisions in the course of the Namaqua-Natal orogeny (Jacobs et al., 2008).

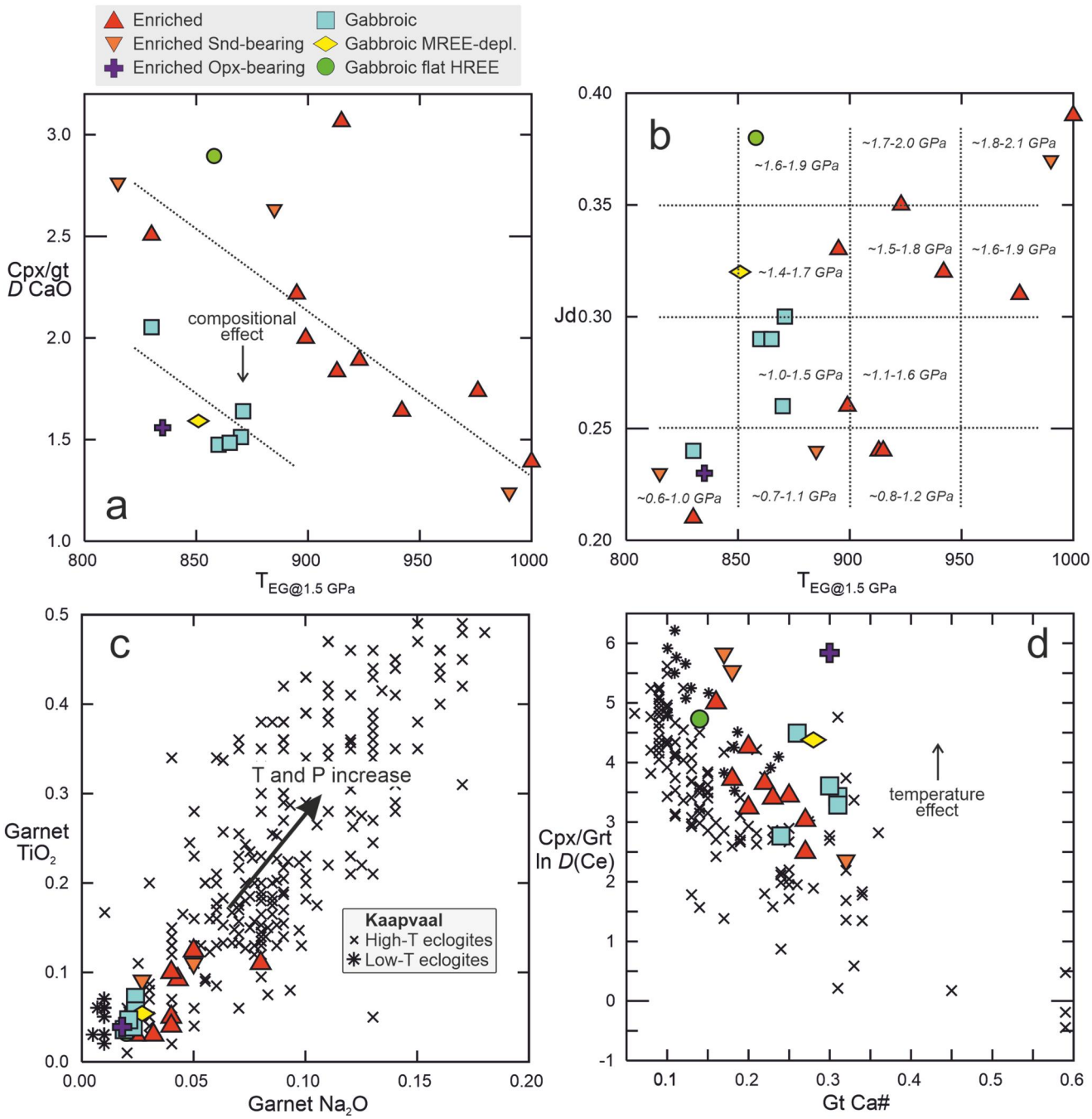

Figure 3. Mineral compositional and temperature distributions for eclogite xenoliths from the Kaapvaal craton margin. (a) Distribution of CaO (wt.%) between clinopyroxene and garnet, and (b) jadeite component (Jd) in clinopyroxene as a function of temperature (°C; from Table 1); arrow in (a) indicates the compositional effect on *D* values at a given temperature. Also shown in (b) are rough pressure estimates based on Jd from Kushiro (1969). (c) TiO_2 as a function of Na_2O content (wt.%) in garnet (data from Tinguely et al. (2008) and le Roex et al. (2020)). (d) Distribution *D* of Ce between clinopyroxene and garnet as a function of garnet grossular component (=Ca#); arrow indicates temperature effect on *D* values at a given Ca#. Shown for comparison in (c) and (d) are high- and low-temperature on-craton eclogites from the Kaapvaal craton (database in Aulbach et al. (2022)).

Mafic material near the Moho has been inferred from geophysical imaging, and suggested to reflect magma underplating in continental margin settings and Precambrian suture zones, such as the NNFB (e.g., O'Reilly & Griffin, 2013; Thybo & Artemieva, 2013). Conversely, the prograde metamorphic origin of deep crustal eclogite xenoliths from the Prieska domain illustrates that mafic material near the Moho may also be subduction-derived.

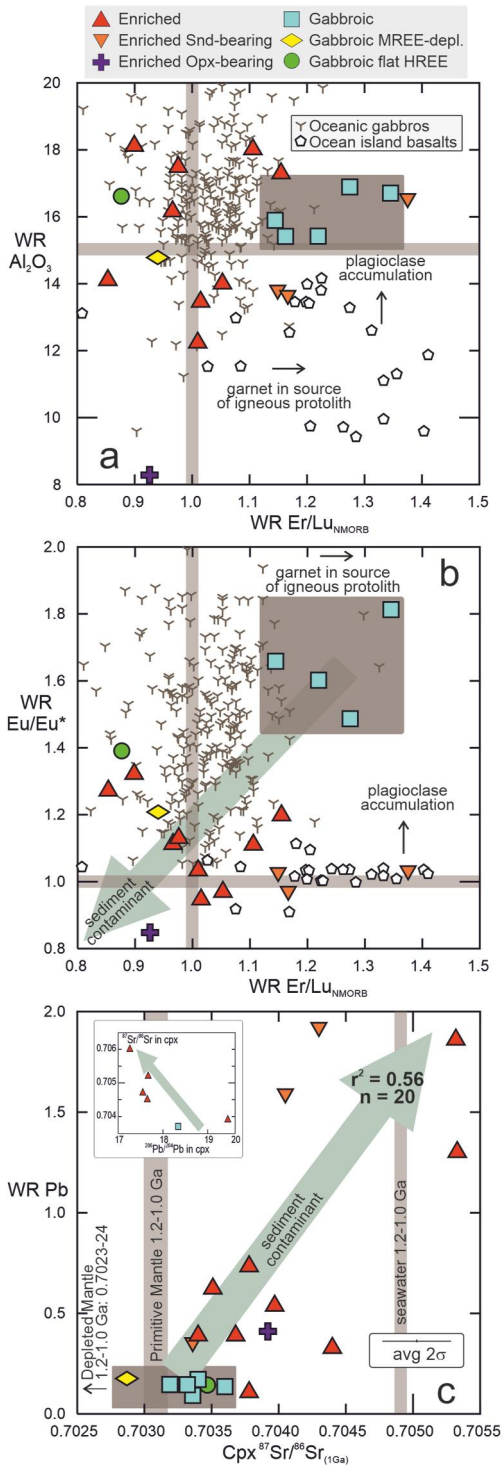

Figure 4.

5.2. Intra-Plate Oceanic Crustal Protoliths for Eclogite Xenoliths From the Kaapvaal Craton Margin

The negative slope in the HREE of most deep crustal eclogites from the Kaapvaal craton margin (Figure 2), captured by low NMORB-normalized Er/Lu (denoted with subscript NMORB), is unlike the flat patterns typically seen in crustal sections from ophiolites, but similar to ratios observed in ocean island basalts (OIBs; Figure 4a). This may indicate that the protolith crystallized from a melt that emanated from a garnet-bearing mantle source, possibly implying partial melting below mature, thick oceanic lithosphere. In contrast to OIBs, however, the gabbroic eclogites are characterized by higher Al_2O_3, which is related to their origin as plagioclase-rich cumulates, consistent with their high Eu/Eu* (Figure 4b). The low end of the narrow range of initial $^{87}Sr/^{86}Sr_{(1\ Ga)}$ (0.7029–0.7036) for gabbroic eclogites compared to enriched eclogites is similar to primitive mantle at 1.2–1.0 Ga, whereas the high end could be explained by interaction with contemporaneous seawater (Figure 4c), as also required by non-mantle $\delta^{18}O$ in several of the samples (Table 1).

While gabbroic eclogite 42223 has non-mantle $\delta^{18}O$ and a positive Eu anomaly that points to its origin as a low-temperature seawater-altered plagioclase-rich cumulate, its HREE pattern is distinctly flat, similar to gabbros formed in spreading ridges (Figure 2c). The orthopyroxene-bearing eclogite 42103 has a flat HREE pattern similar to 42223, though shares the MREE-enriched signature of metasomatized eclogites. It is suggested to have a plagioclase-poor gabbronorite protolith, which helps explain its low Eu/Eu* (<0.85). These two samples may represent part of the original spreading ridge-derived oceanic crust, formed by partial melting of spinel peridotite to shallow levels prior to aging of the oceanic lithosphere.

5.3. Metasomatism by Peridotite-Hybridized Sediment Fluid in a Subduction Mélange

Negative slopes in the HREE (Figure 2b) and $Er/Lu_{NMORB} > 1$ of many enriched eclogites (Figure 4a) suggest a common origin with gabbroic eclogites. However, their LREE-MREE-enrichment, with a break in the slope

Figure 4. Elemental and Sr isotopic proxies to identify protoliths, seawater alteration and sediment signatures in eclogite xenoliths from the Kaapvaal craton margin. (a) Al_2O_3 (wt.%) and (b) Eu/Eu* in reconstructed whole rocks WR (as a proxy for plagioclase accumulation in the eclogites' protoliths) as a function of NMORB-normalized Er/Lu (as a proxy for garnet in the protolith source); NMORB of Gale et al. (2013). Arrow in (b) indicates the muting of plagioclase and garnet signatures due to inferred interaction with a sediment melt or fluid. Gabbros from PetDB (www.earthchem.org/petdb) and ocean island basalts from GEOROC (http://georoc.mpch-mainz.gwdg.de). (c) Initial $^{87}Sr/^{86}Sr$ (at 1 Ga) in clinopyroxene versus Pb concentration (μg/g) in reconstructed whole rocks; average instrumental 2SE and 2σ for multiple spots per sample are 0.00019 and 0.00031, respectively. Range of $^{87}Sr/^{86}Sr$ in seawater at 1.2–1.0 Ga (the main phase of the Namaqua-Natal orogeny) from Shields and Veizer (2002), in Primitive Mantle and Depleted Mantle calculated from present-day values of Workman and Hart (2005) (see Table S2 in Supporting Information S1). Inset shows anticorrelation of measured $^{206}Pb/^{204}Pb$ with $^{87}Sr/^{86}Sr$ (values from le Roex et al. (2020)). Arrows indicate increasing contamination by sediment melt or fluid, while dark gray rectangles encompass the relatively pristine gabbroic eclogites. Note that whole-rock trace-element abundances are only reconstructed when above the detection limit in both garnet and clinopyroxene.

between Gd and Ho (Figure 2b), requires the operation of additional processes. This enriched signature is recognized in both garnet and clinopyroxene (Figure S2 in Supporting Information S1), and therefore independent of the mineral modes applied in bulk rock reconstruction. Moreover, enriched eclogites have lower average Eu/Eu* (1.1), Sr* (1.9), and Pb* (2.5) than gabbroic eclogites (1.7, 8.1, and 14.8, respectively; Table 2). Kimberlite is strongly enriched in incompatible trace elements relative to mafic rocks (e.g. Sr, Nb, Ba, Pb, Th, U) and has elevated $^{87}Sr/^{86}Sr$ (Becker & Le Roex, 2006). Although direct sampling of a kimberlite component in the xenoliths is avoided by reconstructing bulk rocks from mineral compositions, metasomatism by kimberlite-like melt precursory to entrainment is a common phenomenon in eclogite xenoliths (Aulbach, Massuyeau, et al., 2020). Such metasomatism could explain the observed enrichment in many incompatible trace elements and radiogenic Sr. However, further important consequences of kimberlite metasomatism of xenolithic eclogites are the homogenization of $\delta^{18}O$ to mantle values (5.5 ± 0.4‰; Mattey et al., 1994) and a decrease in Li, Cu, and Zn abundances (Aulbach, Massuyeau, et al., 2020). In contrast, deep crustal xenoliths experienced enrichment in incompatible elements, such as Pb, together with enrichment in heavy O, and do not show coupled Li depletion and Th enrichment that characterizes mantle-metasomatized on-craton eclogite xenoliths (Figures 5a and 5b). Finally, kimberlites are prominently linked to TiO_2-enrichment in the lithospheric mantle (e.g., Fitzpayne et al., 2020), whereas six of the 13 enriched eclogites are rutile-free (both in the study of le Roex et al. (2020), and in this study where different subsamples were investigated), implying low total TiO_2 contents. Thus, metasomatism by kimberlite seems an unlikely cause of the observed systematics.

Clinopyroxene in six enriched samples has $\delta^{18}O$ (Table 1) outside the canonical mantle range, and Pb and Li contents in some enriched samples increase with increasing clinopyroxene $\delta^{18}O$ (Figures 5a and 5c). There is a weak negative correlation ($r^2 = 0.34$, $n = 12$) of Eu/Eu* with $^{87}Sr/^{86}Sr_{(1\ Ga)}$ in enriched eclogites (Figure 5d), and they have lower Eu/Eu*, Sr* and Pb* than gabbroic eclogites, as noted above. This suggests that originally stronger anomalies were muted by enrichment. All these observations, including enrichment in isotopically heavy O, may indicate interaction with a seawater-altered sedimentary component. This is further supported by the negative correlation of measured $^{206}Pb/^{204}Pb$ with $^{87}Sr/^{86}Sr$ in clinopyroxene (inset in Figure 4c; data in le Roex et al. (2020)). Clinopyroxene in two enriched eclogites preserve Sr isotopic heterogeneity (Table S2 in Supporting Information S1), with the less radiogenic value overlapping those in gabbroic eclogites and the more radiogenic value in excess of seawater at 1 Ga (Figure 4c), suggesting that complete isotopic equilibrium was not achieved at the relatively low temperatures recorded by the eclogites. As the two samples with the highest $^{87}Sr/^{86}Sr_{(1\ Ga)}$ are characterized not only by high concentration of fluid-mobile elements (Li and Pb), but also of relatively fluid-immobile elements, such as Be and Th (Figure 5e), involvement of a melt or a solute-rich fluid may be indicated.

We consider it significant that 10 of 12 enriched eclogites have higher equilibration temperatures (and inferred pressures) than gabbroic eclogites, consistent also with their higher garnet TiO_2 and Na_2O contents (Figure 3c). Thus, the inferred sediment-derived melt or fluid may have been produced on a prograde path only at deeper and warmer conditions than those recorded by gabbroic eclogites. While Sadofsky and Bebout (2003) find that subducted sediments retain their trace-element inventory to depths of at least 40 km, Albers et al. (2022) observe that SiO_2 and Na_2O are added in metasomatized basalt clasts at 25–30 km depth, along with K_2O, Ba and Rb. This suggests that solute-rich fluids rich in alkalis are already liberated at shallow depth(s) and may explain the presence of sanidine in some of the craton-margin eclogite xenoliths. Similarly, sanidine in orthopyroxene-bearing eclogite xenoliths from the >1.6 Ga Kuruman kimberlite near the western Kaapvaal craton edge was linked to phlogopite- or phengite-bearing protoliths emplaced in a convergent margin (Schmickler et al., 2004) that must, however, have been older than the 1.2–1.0 Ga Namaqua-Natal orogeny. In enriched eclogites, SiO_2 and Na_2O contents are on average only slightly higher (47.3 and 2.4 wt.%, respectively) than in pristine eclogites (46.0 and 2.0 wt.%, respectively; Table 2), and they are not enriched in Al_2O_3. They may therefore have been metasomatized at depths where the ability of fluids to form aluminosilicate components was still limited compared to deeper forearc or subarc conditions (Manning, 2004).

Finally, nearly half of the enriched eclogites are rutile-free, whereas all pristine gabbroic eclogites contain accessory rutile. This conclusion is based on xenolith fragments studied by le Roex et al. (2020) and on different fragments used in the present study. Therefore, this is not due to a sectioning effect, where accessory rutile is not necessarily exposed. The TiO_2 solubility in a melt increases as it becomes less felsic (Hayden & Watson, 2007). Thus, the inferred sediment-derived melt or fluid may have become TiO_2-undersaturated during hybridization with ultramafic portions of the slab before interacting with the oceanic crust subsequently sampled as rutile-free

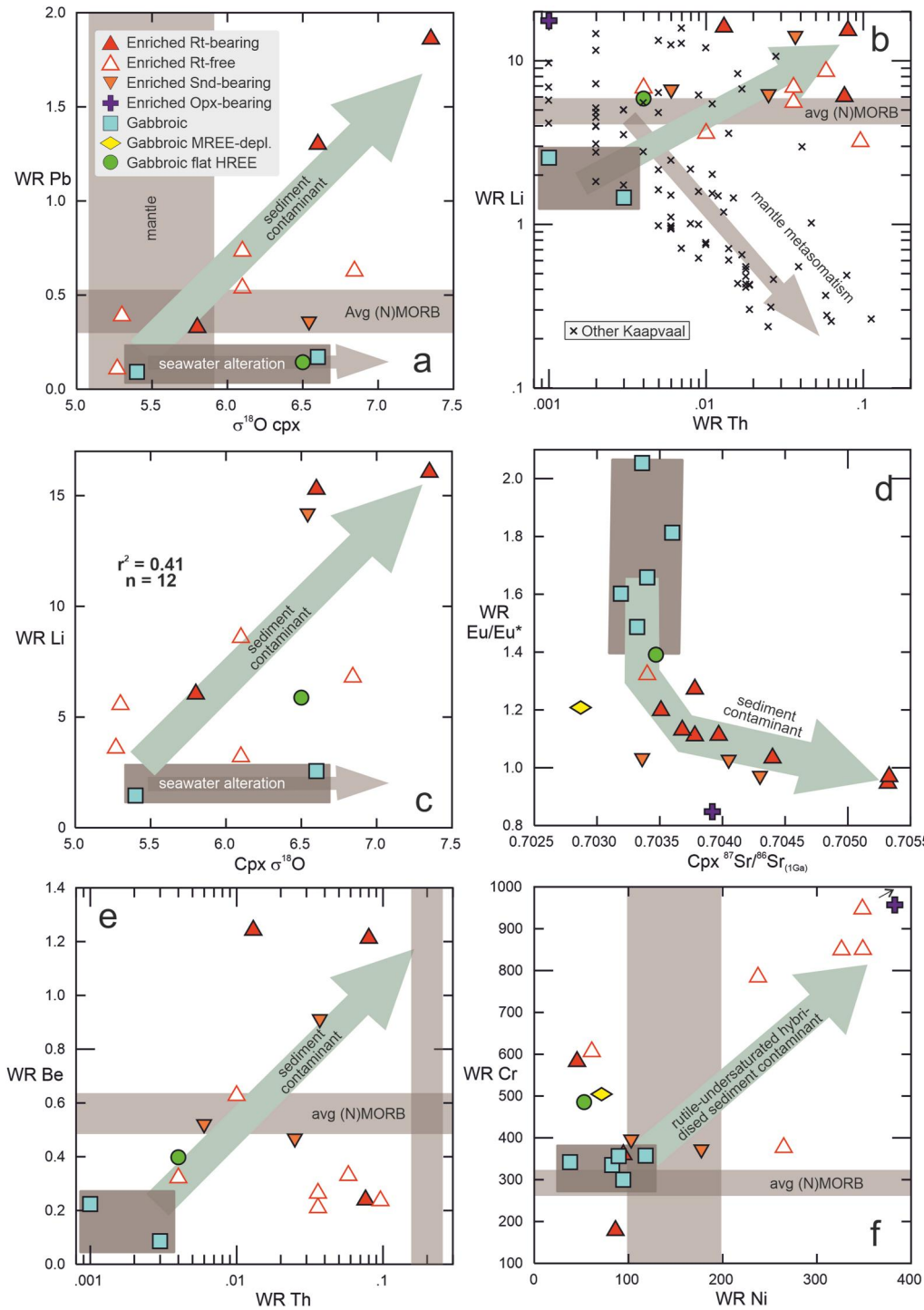

Figure 5. Major and trace element proxies to identify sediment signatures in eclogite xenoliths from the Kaapvaal craton margin. (a) Pb concentration (μg/g) in reconstructed whole rocks WR as a function of $\delta^{18}O$ in clinopyroxene. Mantle range from Mattey et al. (1994). Suggested trends of low-temperature seawater alteration and of interaction with seawater-altered sediment-derived fluid are also shown. (b) Li concentration (μg/g) as a function of Th concentration (μg/g) in reconstructed whole rocks. Note different trends for interaction with sediment contaminant and with kimberlite-like melt which metasomatized on-craton Kaapvaal eclogite xenoliths (references as in Figure 3). (c) Li concentration (μg/g) in reconstructed whole rocks as a function of $\delta^{18}O$ in clinopyroxene. (d) Eu/Eu* in reconstructed whole rocks as a function of initial $^{87}Sr/^{86}Sr$ (at 1 Ga) in clinopyroxene. (e) Be as a function of Th concentration (μg/g) and (f) Cr as a function of Ni concentration (μg/g) in reconstructed whole rocks, indicating the enrichment of relatively fluid-immobile elements, and the increase in (ultra)mafic components in rutile-free eclogites, the latter suggestive of interaction with a hybridized rutile-undersaturated melt or solute-rich fluid. Dark gray rectangles encompass the relatively pristine gabbroic eclogites. Range of average (N)MORB (gray bars) represents average compositions from Sun and McDonough (1989), Arevalo and McDonough (2010), and Gale et al. (2013). Note that whole-rock trace-element abundances are only reconstructed when above the detection limit in both garnet and clinopyroxene.

eclogites. This can explain why rutile-free eclogites have higher MgO (average 12.4 wt.%, $n = 6$), Cr (740 μg/g) and Ni (260 μg/g) contents than rutile-bearing ones (average 9.7 wt.%, 400 and 110 μg/g, respectively) (Table 2; Figure 5f). This excludes the orthopyroxene-bearing sample, which inherited these signatures from a deep oceanic crustal troctolite, as discussed above. Rutile-free eclogites are also less enriched in Li, Pb, and radiogenic Sr, suggesting dilution of these signatures during hybridization of the sedimentary melt/fluid contaminant with peridotite having a mantle isotopic composition at the time of subduction.

Taken together, these varied signatures of continental sediment and of sediment hybridized with ultramafic rocks can be produced in a subduction mélange setting.

5.4. Low Oxygen Fugacity of Mesoproterozoic Deep Continental Crust

Oxygen fugacity (fO_2) controls the speciation of multivalent elements, and therefore their behavior in the presence of fluid or melt and their capacity to oxidize the supra-subduction zone (e.g., Evans et al., 2012). As a consequence, fO_2 also controls the economic concentrations of metals (e.g., Cu, Au), where oxidizing conditions suppress the early formation of sulphide-bearing cumulates, which would otherwise scavenge metals from the system (Evans & Tomkins, 2011). Craton margins and collisional belts are tectonic weak zones and pathways for incompatible element-rich oxidizing magmas (e.g., Lenardic et al., 2003; Tappe et al., 2020), and this is true also for the NNFB, which was multiply intruded by lamproites and then kimberlites (Becker & Le Roex, 2006). They should therefore represent preferred loci of metallogenesis (e.g., Mole et al., 2015). Eclogite xenoliths from the NNFB sample the deep crust-mantle transition and can therefore provide insights into the redox state at this critical boundary.

Six pristine reconstructed bulk gabbroic eclogites show a weak negative correlation of $Fe^{3+}/\Sigma Fe$ with Eu/Eu* ($r^2 = 0.45$; Figure 6a). This would be consistent with exclusion of Fe^{3+}, which is more incompatible than Fe^{2+}, due to accumulation of olivine and plagioclase during formation of the igneous protolith. While enriched eclogites encompass $Fe^{3+}/\Sigma Fe$ of gabbroic eclogites, it may be significant that those with some of the highest abundances of Pb, which is enriched in the continental crust (Rudnick & Gao, 2014) relative to the mantle (Salters & Stracke, 2004), plot at the high-$Fe^{3+}/\Sigma Fe$ end (Figure 6b). Although four samples with the highest $Fe^{3+}/\Sigma Fe$ (0.08 ± 0.01) are restricted to fO_2 >FMQ-1.5, enriched and unenriched eclogites can be considered to have identical bulk $Fe^{3+}/\Sigma Fe$ and fO_2 within the uncertainties (Figure 6c), suggesting no significant change in $Fe^{3+}/\Sigma Fe$ or fO_2 during metasomatism. Moreover, as in on-craton eclogite xenoliths (Aulbach et al., 2022), $Fe^{3+}/\Sigma Fe$ and fO_2 are decoupled, and neither is associated with mineral modal abundances, illustrating the complex relationship between extensive and intensive proxies of oxygen in metamorphic rocks.

Bearing in mind that fO_2 estimates are maxima for any sample that is silica-undersaturated, $\Delta \log fO_2$(FMQ) estimates in craton-margin eclogite xenoliths vary from -3.1 ± 1.0 to -0.5 ± 0.7. The average fO_2 of the subduction-modified deep crust-mantle transition beneath the NNFB is higher than that of most eclogite xenoliths from the Kaapvaal craton, but lower than estimates for modern MORB (estimates vary between FMQ-0.4 ± 0.4 and 0.6 ± 0.3; Cottrell et al., 2022; Frost & McCammon, 2008; Nicklas et al., 2019) (Figure 6c). They are on average slightly higher than those determined for oceanic crust following a prograde metamorphic path sampled as orogenic eclogites from western Tianshan, with FMQ-1.9 to −2.5 at ∼2.5 GPa and 500–575°C (Tao et al., 2020) (Figure 6d). This supports the notion that subducting oceanic crust becomes more reduced with depth (Aulbach et al., 2017; Stagno et al., 2015). Average fO_2 estimates (-1.5 ± 0.7) for the deep crust below the NNFB are significantly more reduced than most crustal components entering modern subduction zones (metasediment FMQ+2.5 to +3; blueschists FMQ > 0, epidote eclogite FMQ+4.5, eclogite <0 to +2.5; Cannaò & Malaspina, 2018). They are also more reduced than arc front magmas (FMQ > 0.9; Cottrell et al., 2022; Evans et al., 2012) and deep intraoceanic arc crust (FMQ + 0.4 to +2.3 at ∼1 GPa; Bucholz & Kelemen, 2019), but partially overlap Neoproterozoic arc crust with FMQ-2.4 to FMQ + 0.7 (Zhang et al., 2017).

All sulfur in melts in equilibrium with deep crustal eclogites would be present exclusively as S^{2-} at their pressures and oxygen fugacities (Figure 6d). This precludes a role for the transfer of sulfate from the subduction-modified oceanic crust in oxidizing the overlying lithosphere, at least during formation of the 1.2–1.0 Ga NNFB, and is consistent with findings that the paucity of oxidized magmas prior to Neoproterozoic deep ocean oxygenation reflects the reduced nature of slab-derived components (Evans & Tomkins, 2011).

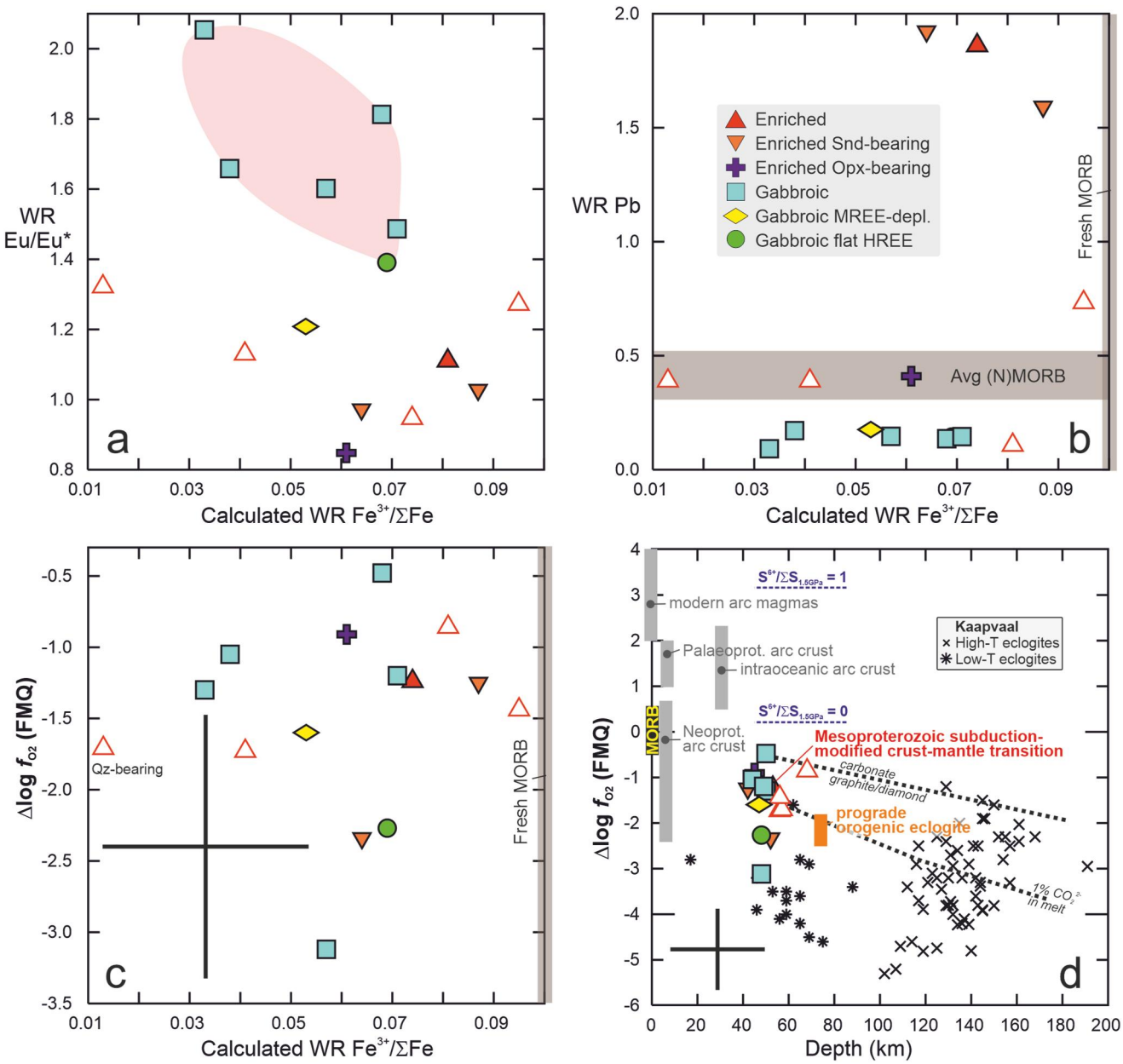

Figure 6. Bulk-rock $Fe^{3+}/\Sigma Fe$ and fO_2 estimates for eclogite xenoliths from the Kaapvaal craton margin. (a) Eu/Eu* and (b) Pb abundances (μg/g) as a function of $Fe^{3+}/\Sigma Fe$ in reconstructed whole rocks WR; six pristine gabbroic eclogites showing a weak anticorrelation are highlighted in (a). Fresh MORB in (b) from Berry et al. (2018), average (N)MORB compositions as in Figure 5. Oxygen fugacity (fO_2) relative to the Fayalite-Magnetite-Quartz buffer (FMQ) as a function of (c) $Fe^{3+}/\Sigma Fe$ in reconstructed whole rocks and (d) depth (km). The single quartz (qz)-bearing eclogite is indicated; these fO_2 values are maxima for any sample that is not quartz-saturated. Carbonate versus graphite/diamond boundary (uncertainty 0.6 log units) from Stagno et al. (2015) extrapolated to 50 km depth, stability of melt with 1% CO_2 from Stagno et al. (2013). Fraction of oxidized sulfur ($S^{6+}/\Sigma S$) in melts at 1.5 GPa and 950°C, similar to conditions recorded by deep crustal eclogites, from Matjuschkin et al. (2016). Shown for comparison are Kaapvaal eclogite xenoliths from the literature (database in Aulbach et al. (2022)), range of estimates for modern oceanic crust (MORB) bracketed by Frost and McCammon (2008) and Nicklas et al. (2019), range of modern arc magmas (Evans et al., 2012), intra-oceanic arc crust at 1 GPa (Bucholz & Kelemen, 2019), Neoproterozoic arc crust (Zhang et al., 2017), Paleoproterozoic arc crust (Meng et al., 2021) and orogenic eclogite under prograde metamorphic conditions (Tao et al., 2020). Average fully propagated 1σ uncertainties on $Fe^{3+}/\Sigma Fe$ and $\Delta \log fO_2$(FMQ) from Table 1 and on depth assuming a 100°C uncertainty in temperature along a conductive geotherm are shown as error bars in (c) and (d).

6. Summary and Conclusions

We report in situ trace-element, clinopyroxene $^{87}Sr/^{86}Sr$ and garnet $Fe^{3+}/\Sigma Fe$ of previously investigated kimberlite-borne eclogite xenoliths from the deep crust-mantle transition below the NNFB at the southwestern Kaapvaal craton margin (le Roex et al., 2020; Tinguely et al., 2008). Low combined TiO_2-Na_2O contents in garnet compared to deep-seated on-craton eclogite xenoliths support their unusual, shallow origin. Our study of the physicochemical characteristics of these eclogites lead to the following main conclusions:

1. Pristine "gabbroic" eclogites with pronounced positive Eu, Sr, and Pb anomalies, show a distinct garnet source signature for formation of their igneous protoliths, proxied by NMORB-normalized Er/Lu > 1. This suggests formation of the bulk of the suite by crystal accumulation in oceanic crust from melts generated beneath mature oceanic lithosphere, followed by metamorphism during the Namaqua-Natal orogeny. Their clinopyroxenes have $^{87}Sr/^{86}Sr_{(1\ Ga)}$ of 0.7029–0.7036 and $\delta^{18}O$ of 5.3–7.4, consistent with formation from an approximately primitive mantle source and seawater alteration in Mesoproterozoic time.
2. Enriched eclogites are distinct from gabbroic eclogites in their higher average temperatures (915 vs. 860°C), Nd/Yb (3.8 vs. 0.5), Th abundances (0.0031 vs. 0.0018 μg/g) and $^{87}Sr/^{86}Sr_{(1Ga)}$ in clinopyroxene (up to 0.70533). Moreover, they show increasing bulk-rock Li and Pb with increasing $\delta^{18}O$ in clinopyroxene, accompanied by a muting of Eu-Sr-Pb anomalies. This suggests interaction with a melt or siliceous fluid sourced from seawater-altered oceanic sediment, and shows that mafic crust near the Moho detected by geophysical imaging need not have formed by basalt underplating.
3. Rutile-free enriched eclogites have higher MgO (average 12.4 wt.%), Cr (740 μg/g) and Ni (260 μg/g) contents than rutile-bearing samples (9.7 wt.%, 400 and 110 μg/g, respectively). This suggests that the inferred sedimentary contaminant became rutile-undersaturated after hybridization with (ultra)mafic material, allowing it to assimilate rutile upon interaction with the oceanic crust. Interaction of oceanic crust, sediment and (ultra)mafic material can be explained by a subduction mélange setting.
4. Garnet $Fe^{3+}/\Sigma Fe$ in deep crustal eclogites is extremely low (0.01–0.04, ±0.01 1σ) due to their cumulate origin (hence preferred exclusion of Fe^{3+}) and to preferred partitioning of Fe^{3+} into coexisting clinopyroxene at low temperatures. Calculated bulk $Fe^{3+}/\Sigma Fe$ values are mostly sub-MORB (<0.08), but a modest increase during interaction with sediment-derived melt is suggested for some enriched eclogites.
5. Average $\Delta \log fO_2$(FMQ) of -3.1 ± 1.0 to -0.5 ± 0.7 in deep crustal eclogites is higher than in deep-seated on-craton eclogite xenoliths, but lower than MORB, consistent with a general decrease in eclogite fO_2 with depth. This range of fO_2 is not permissive of sulfate stabilization in melts in equilibrium with deep crustal eclogites. Therefore, the transfer of redox budget from the Midproterozoic oceanic crust during NNFB formation was probably limited, and would not have played a role in the oxidation of the supra-subduction zone lithosphere. This adds to growing evidence from modern orogenic to on-craton eclogites that oxygen fugacity in subducted oceanic crust decreases with depth and beyond ~40 km is a sink rather than a source of oxygen.

Conflict of Interest

The authors declare no conflicts of interest relevant to this study.

Data Availability Statement

All new data used in this paper (mineral trace element data, measured clinopyroxene $^{87}Sr/^{86}Sr$, garnet $Fe^{3+}/\Sigma Fe$) are available at (Aulbach et al., 2023).

Acknowledgments
We thank two anonymous reviewers and the associate editor for their comments, which significantly improved the accuracy and clarity of the paper, as well as the editor, Mark Dekkers, for seamless handling. The Deutsche Forschungsgemeinschaft is gratefully acknowledged for funding to SA (DFG Project numbers 397589446 and 467591567). FIERCE is financially supported by the Wilhelm and Else Heraeus Foundation and by the Deutsche Forschungsgemeinschaft (DFG: INST 161/921-1 FUGG, INST 161/923-1 FUGG, and INST 161/1073-1 FUGG), which is gratefully acknowledged. This is FIERCE contribution No.152. Open Access funding enabled and organized by Projekt DEAL.

References

Albers, E., Shervais, J. W., Hansen, C. T., Ichiyama, Y., & Fryer, P. (2022). Shallow depth, substantial change: Fluid-metasomatism causes major compositional modifications of subducted volcanics (Mariana Forearc). *Frontiers in Earth Science*, *10*. https://doi.org/10.3389/feart.2022.826312

Arevalo, R., & McDonough, W. F. (2010). Chemical variations and regional diversity observed in MORB. *Chemical Geology*, *271*(1–2), 70–85. https://doi.org/10.1016/j.chemgeo.2009.12.013

Aulbach, S. (2020). Temperature-dependent rutile solubility in garnet and clinopyroxene from mantle eclogite: Implications for continental crust formation and V-based oxybarometry. *Journal of Petrology*, *61*(6), egaa065. https://doi.org/10.1093/petrology/egaa065

Aulbach, S., Gerdes, A., & Viljoen, K. S. (2016). Formation of diamondiferous kyanite-eclogite in a subduction melange. *Geochimica et Cosmochimica Acta*, *179*, 156–176. https://doi.org/10.1016/j.gca.2016.01.038

Aulbach, S., Höfer, H. E., & Gerdes, A. (2023). Mineral trace element data, measured clinopyroxene $^{87}Sr/^{86}Sr$, garnet $Fe^{3+}/\Sigma Fe$ for eclogite xenoliths from the Prieska domain at the western Kaapvaal craton margin (South Africa) version 1.0 [Dataset]. Interdisciplinary Earth Data Alliance (IEDA). https://doi.org/10.60520/IEDA/113077

Aulbach, S., Massuyeau, M., Garber, J. M., Gerdes, A., Heaman, L. M., & Viljoen, K. S. (2020). Ultramafic carbonated melt- and auto-metasomatism in mantle eclogites: Compositional effects and geophysical consequences. *Geochemistry, Geophysics, Geosystems*, *21*(5), e2019GC008774. https://doi.org/10.1029/2019gc008774

Aulbach, S., Viljoen, K. S., & Gerdes, A. (2020). Diamondiferous and barren eclogites and pyroxenites from the western Kaapvaal craton record subduction processes and mantle metasomatism, respectively. *Lithos*, *368*, 105588. https://doi.org/10.1016/j.lithos.2020.105588

Aulbach, S., Woodland, A. B., Stagno, V., Korsakov, A. V., Mikhailenko, D., & Golovin, A. (2022). Fe^{3+} distribution and $Fe^{3+}/\Sigma Fe$-oxygen fugacity variations in kimberlite-borne eclogite xenoliths, with comments on clinopyroxene-garnet oxy-thermobarometry. *Journal of Petrology*, *63*(8), egac076. https://doi.org/10.1093/petrology/egac076

Aulbach, S., Woodland, A. B., Vasilyev, P., Galvez, M. E., & Viljoen, K. S. (2017). Effects of low-pressure igneous processes and subduction on $Fe^{3+}/\Sigma Fe$ and redox state of mantle eclogites from Lace (Kaapvaal craton). *Earth and Planetary Science Letters*, *474*, 283–295. https://doi.org/10.1016/j.epsl.2017.06.030

Becker, M., & Le Roex, A. P. (2006). Geochemistry of South African on- and off-craton, Group I and Group II kimberlites: Petrogenesis and source region evolution. *Journal of Petrology*, *47*(4), 673–703. https://doi.org/10.1093/petrology/egi089

Benoit, M., Polvé, M., & Ceuleneer, G. (1996). Trace element and isotopic characterization of mafic cumulates in a fossil mantle diapir (Oman ophiolite). *Chemical Geology*, *134*(1–3), 199–214. https://doi.org/10.1016/s0009-2541(96)00087-3

Berry, A. J., Stewart, G. A., O'Neill, H. S. C., Mallmann, G., & Mosselmans, J. F. W. (2018). A re-assessment of the oxidation state of iron in MORB glasses. *Earth and Planetary Science Letters*, *483*, 114–123. https://doi.org/10.1016/j.epsl.2017.11.032

Borfecchia, E., Mino, L., Gianolio, D., Groppo, C., Malaspina, N., Martinez-Criado, G., et al. (2012). Iron oxidation state in garnet from a subduction setting: A micro-XANES and electron microprobe ("flank method") comparative study. *Journal of Analytical Atomic Spectrometry*, *27*(10), 1725–1733. https://doi.org/10.1039/C2JA30149K

Bucholz, C. E., & Kelemen, P. B. (2019). Oxygen fugacity at the base of the Talkeetna arc, Alaska. *Contributions to Mineralogy and Petrology*, *174*(10), 79. https://doi.org/10.1007/s00410-019-1609-z

Cannaò, E., & Malaspina, N. (2018). From oceanic to continental subduction: Implications for the geochemical and redox evolution of the supra-subduction mantle. *Geosphere*, *14*(6), 2311–2336. https://doi.org/10.1130/GES01597.1

Cottrell, E., Birner, S. K., Brounce, M., Davis, F. A., Waters, L. E., & Kelley, K. A. (2022). Oxygen fugacity across tectonic settings. In *Magma redox geochemistry* (pp. 33–61). https://doi.org/10.1002/9781119473206.ch3

Creighton, S. (2009). The influence of mantle metasomatism on the oxidation state of the lithospheric mantle. PhD Thesis (p. 122). University of Alberta.

Evans, K. A., Elburg, M. A., & Kamenetsky, V. S. (2012). Oxidation state of subarc mantle. *Geology*, *40*(9), 783–786. https://doi.org/10.1130/g33037.1

Evans, K. A., & Tomkins, A. G. (2011). The relationship between subduction zone redox budget and arc magma fertility. *Earth and Planetary Science Letters*, *308*(3–4), 401–409. https://doi.org/10.1016/j.epsl.2011.06.009

Fitzpayne, A., Giuliani, A., Hergt, J., Woodhead, J. D., & Maas, R. (2020). Isotopic analyses of clinopyroxenes demonstrate the effects of kimberlite melt metasomatism upon the lithospheric mantle. *Lithos*, *370–371*, 105595. https://doi.org/10.1016/j.lithos.2020.105595

Frost, D. J., & McCammon, C. A. (2008). The redox state of Earth's mantle. *Annual Review of Earth and Planetary Sciences*, *36*(1), 389–420. https://doi.org/10.1146/annurev.earth.36.031207.124322

Gale, A., Dalton, C. A., Langmuir, C. H., Su, Y., & Schilling, J.-G. (2013). The mean composition of ocean ridge basalts. *Geochemistry, Geophysics, Geosystems*, *14*(3), 489–518. https://doi.org/10.1029/2012gc004334

Griffin, W. L., Powell, W. J., Pearson, N. J., & O'Reilly, S. Y. (2008). A2. GLITTER: Data reduction software for laser ablation ICP–MS. In P. Sylvester (Ed.), *Laser ablation-ICPMS in the Earth sciences: Current practices and outstanding issues* (p. 356). Mineralogical Association of Canada.

Hayden, L. A., & Watson, E. B. (2007). Rutile saturation in hydrous siliceous melts and its bearing on Ti-thermometry of quartz and zircon. *Earth and Planetary Science Letters*, *258*(3–4), 561–568. https://doi.org/10.1016/j.epsl.2007.04.020

Höfer, H. E., & Brey, G. P. (2007). The iron oxidation state of garnet by electron microprobe: Its determination with the flank method combined with major-element analysis. *American Mineralogist*, *92*(5–6), 873–885. https://doi.org/10.2138/am.2007.2390

Hofmann, A. W. (1997). Mantle geochemistry: The message from oceanic volcanism. *Nature*, *385*(6613), 219–229. https://doi.org/10.1038/385219a0

Ireland, T. R., Rudnick, R. L., & Spetsius, Z. (1994). Trace elements in diamond inclusions from eclogites reveal link to Archean granites. *Earth and Planetary Science Letters*, *128*(3–4), 199–213. https://doi.org/10.1016/0012-821x(94)90145-7

Jacob, D. E. (2004). Nature and origin of eclogite xenoliths from kimberlites. *Lithos*, *77*(1–4), 295–316. https://doi.org/10.1016/j.lithos.2004.03.038

Jacobs, J., Pisarevsky, S., Thomas, R. J., & Becker, T. (2008). The Kalahari Craton during the assembly and dispersal of Rodinia. *Precambrian Research*, *160*(1–2), 142–158. https://doi.org/10.1016/j.precamres.2007.04.022

Klemme, S., Prowatke, S., Hametner, K., & Gunther, D. (2005). Partitioning of trace elements between rutile and silicate melts: Implications for subduction zones. *Geochimica et Cosmochimica Acta*, *69*(9), 2361–2371. https://doi.org/10.1016/j.gca.2004.11.015

Kushiro, I. (1969). Clinopyroxene solid solutions formed by reactions between diopside and plagioclase at high pressures. In *Mineralogical society of America special paper* (Vol. 2, pp. 179–191).

Lenardic, A., Moresi, L. N., & Muhlhaus, H. (2003). Longevity and stability of cratonic lithosphere: Insights from numerical simulations of coupled mantle convection and continental tectonics. *Journal of Geophysical Research: Solid Earth*, *108*(B6), 2303. https://doi.org/10.1029/2002jb001859

Le Roex, A., Tinguely, C., & Gregoire, M. (2020). Eclogite and garnet pyroxenite xenoliths from kimberlites emplaced along the southern margin of the Kaapvaal Craton, southern Africa: Mantle or lower crustal fragments? *Journal of Petrology*, *61*(4), egaa040. https://doi.org/10.1093/petrology/egaa040

Malaspina, N., Langenhorst, F., Tumiati, S., Campione, M., Frezzotti, M. L., & Poli, S. (2017). The redox budget of crust-derived fluid phases at the slab-mantle interface. *Geochimica et Cosmochimica Acta*, *209*, 70–84. https://doi.org/10.1016/j.gca.2017.04.004

Malaspina, N., Poli, S., & Fumagalli, P. (2009). The oxidation state of metasomatized mantle wedge: Insights from C–O–H-bearing garnet peridotite. *Journal of Petrology*, *50*(8), 1533–1552. https://doi.org/10.1093/petrology/egp040

Malaspina, N., Scambelluri, M., Poli, S., Van Roermund, H. L. M., & Langenhorst, F. (2010). The oxidation state of mantle wedge majoritic garnet websterites metasomatised by C-bearing subduction fluids. *Earth and Planetary Science Letters*, *298*(3–4), 417–426. https://doi.org/10.1016/j.epsl.2010.08.022

Manning, C. E. (2004). The chemistry of subduction-zone fluids. *Earth and Planetary Science Letters*, *223*(1–2), 1–16. https://doi.org/10.1016/j.epsl.2004.04.030

Matjuschkin, V., Blundy, J. D., & Brooker, R. A. (2016). The effect of pressure on sulphur speciation in mid- to deep-crustal arc magmas and implications for the formation of porphyry copper deposits. *Contributions to Mineralogy and Petrology*, *171*(7), 66. https://doi.org/10.1007/s00410-016-1274-4

Mattey, D., Lowry, D., & Macpherson, C. (1994). Oxygen-isotope composition of mantle peridotite. *Earth and Planetary Science Letters*, *128*(3–4), 231–241. https://doi.org/10.1016/0012-821x(94)90147-3

McDonough, W. F., & Sun, S.-S. (1995). The composition of the Earth: Chemical evolution of the mantle. *Chemical Geology*, *120*(3-4), 223–253.

McGuire, A. V., Francis, C. A., & Dyar, M. D. (1992). Mineral standards for electron microprobe analysis of oxygen. *American Mineralogist*, *77*, 1087–1091.

Meng, X., Kleinsasser, J. M., Richards, J. P., Tapster, S. R., Jugo, P. J., Simon, A. C., et al. (2021). Oxidized sulfur-rich arc magmas formed porphyry Cu deposits by 1.88 Ga. *Nature Communications*, *12*(1), 2189. https://doi.org/10.1038/s41467-021-22349-z

Mole, D. R., Fiorentini, M. L., Cassidy, K. F., Kirkland, C. L., Thebaud, N., McCuaig, T. C., et al. (2015). Crustal evolution, intra-cratonic architecture and the metallogeny of an Archaean craton. In G. R. T. Jenkin, P. A. J. Lusty, I. McDonald, M. P. Smith, A. J. Boyce, & J. J. Wilkinson (Eds.), *Ore deposits in an evolving Earth* (pp. 23–80). Geological Society Special Publications.

Nguuri, T. K., Group, K. S., Gore, J., James, D. E., Webb, S. J., Wright, C., et al. (2001). Crustal structure beneath southern Africa and its implications for the formation and evolution of the Kaapvaal and Zimbabwe cratons. *Geophysical Research Letters*, *28*(13), 2501–2504. https://doi.org/10.1029/2000gl012587

Nicklas, R. W., Puchtel, I. S., Ash, R. D., Piccoli, H. M., Hanski, E., Nisbet, E. G., et al. (2019). Secular mantle oxidation across the Archean-Proterozoic boundary: Evidence from V partitioning in komatiites and picrites. *Geochimica et Cosmochimica Acta*, *250*, 49–75. https://doi.org/10.1016/j.gca.2019.01.037

O'Reilly, S. Y., & Griffin, W. L. (2013). Moho vs crust-mantle boundary: Evolution of an idea. *Tectonophysics*, *609*, 535–546. https://doi.org/10.1016/j.tecto.2012.12.031

Pearson, D. G., Scott, J. M., Liu, J., Schaeffer, A., Wang, L. H., van Hunen, J., et al. (2021). Deep continental roots and cratons. *Nature*, *596*(7871), 199–210. https://doi.org/10.1038/s41586-021-03600-5

Rankenburg, K., Lassiter, J. C., & Brey, G. (2004). Origin of megacrysts in volcanic rocks of the Cameroon volcanic chain—Constraints on magma genesis and crustal contamination, Contributions to mineralogy and petrology. *Contributions to Mineralogy and Petrology*, *147*(2), 129–144. https://doi.org/10.1007/s00410-003-0534-2

Rudnick, R. L., & Gao, S. (2014). Composition of the continental crust. In H. D. Holland, & K. K. Turekian (Eds.), *Treatise on geochemistry—The crust* (pp. 1–51). Elsevier Ltd.

Sadofsky, S. J., & Bebout, G. E. (2003). Record of forearc devolatilization in low-T, high-P/T metasedimentary suites: Significance for models of convergent margin chemical cycling. *Geochemistry, Geophysics, Geosystems*, *4*(4), 9003. https://doi.org/10.1029/2002GC000412

Salters, V. J. M., & Stracke, A. (2004). Composition of the depleted mantle. *Geochemistry, Geophysics, Geosystems*, *5*, Q05B07. https://doi.org/10.1029/2003gc000597

Schmickler, B., Jacob, D. E., & Foley, S. F. (2004). Eclogite xenoliths from the Kuruman kimberlites, South Africa: Geochemical fingerprinting of deep subduction and cumulate processes. *Lithos*, *75*(1–2), 173–207. https://doi.org/10.1016/j.lithos.2003.12.012

Schmitz, M. D., & Bowring, S. A. (2003). Ultrahigh-temperature metamorphism in the lower crust during Neoarchean Ventersdorp rifting and magmatism, Kaapvaal Craton, southern Africa. *Geological Society of America Bulletin*, *115*(5), 533–548. https://doi.org/10.1130/0016-7606(2003)115<0533:umitlc>2.0.co;2

Shields, G., & Veizer, J. (2002). Precambrian marine carbonate isotope database: Version 1.1. *Geochemistry, Geophysics, Geosystems*, *3*(6). https://doi.org/10.1029/2001gc000266

Smart, K. A., Chacko, T., Simonetti, A., Sharp, Z. D., & Heaman, L. M. (2014). A record of Paleoproterozoic subduction preserved in the Northern Slave cratonic mantle: Sr-Pb-O isotope and trace-element investigations of eclogite xenoliths from the Jericho and Muskox kimberlites. *Journal of Petrology*, *55*(3), 549–583. https://doi.org/10.1093/petrology/egt077

Smart, K. A., Tappe, S., Woodland, A. B., Greyling, D. R., Harris, C., & Gussone, N. (2021). Constraints on Archean crust recycling and the origin of mantle redox variability from the $\delta^{44}/^{40}$Ca—δ^{18}O—fO_2 signatures of cratonic eclogites. *Earth and Planetary Science Letters*, *556*, 116720. https://doi.org/10.1016/j.epsl.2020.116720

Smart, K. A., Tappe, S., Woodland, A. B., Harris, C., Corcoran, L., & Simonetti, A. (2021). Metasomatized eclogite xenoliths from the central Kaapvaal craton as probes of a seismic mid-lithospheric discontinuity. *Chemical Geology*, *578*, 120286. https://doi.org/10.1016/j.chemgeo.2021.120286

Smith, C. B., Clark, T. C., Barton, E. S., & Bristow, J. W. (1994). Emplacement ages of kimberlite occurrences in the Prieska region, southwest border of the Kaapvaal craton, South Africa. *Chemical Geology*, *113*(1–2), 149–169. https://doi.org/10.1016/0009-2541(94)90010-8

Stagno, V., Frost, D. J., McCammon, C. A., Mohseni, H., & Fei, Y. (2015). The oxygen fugacity at which graphite or diamond forms from carbonate-bearing melts in eclogitic rocks. *Contributions to Mineralogy and Petrology*, *169*(2), 16. https://doi.org/10.1007/s00410-015-1111-1

Stagno, V., Ojwang, D. O., McCammon, C. A., & Frost, D. J. (2013). The oxidation state of the mantle and the extraction of carbon from Earth's interior. *Nature*, *493*(7430), 84–88. https://doi.org/10.1038/nature11679

Sun, S.-S., & McDonough, W. F. (1989). Chemical and isotopic systematics of oceanic basalts: Implications for mantle compositions and processes. In N. M. Saunders, & A. D. Norris (Eds.), *Geological society special publication* (pp. 313–345).

Tang, M., Lee, C. T. A., Chen, K., Erdman, M., Costin, G., & Jiang, H. H. (2019). Nb/Ta systematics in arc magma differentiation and the role of arclogites in continent formation. *Nature Communications*, *10*(1), 235. https://doi.org/10.1038/s41467-018-08198-3

Tao, R., Zhang, L., Tian, M., Zhu, J., Liu, X., Liu, J., et al. (2018). Formation of abiotic hydrocarbon from reduction of carbonate in subduction zones: Constraints from petrological observation and experimental simulation. *Geochimica et Cosmochimica Acta*, *239*, 390–408. https://doi.org/10.1016/j.gca.2018.08.008

Tao, R., Zhang, L., & Zhang, L. (2020). Redox evolution of western Tianshan subduction zone and its effect on deep carbon cycle. *Geoscience Frontiers*, *11*(3), 915–924. https://doi.org/10.1016/j.gsf.2019.09.007

Tappe, S., Smart, K. A., Pearson, D. G., Steenfelt, A., & Simonetti, A. (2011). Craton formation in Late Archean subduction zones revealed by first Greenland eclogites. *Geology*, *39*(12), 1103–1106. https://doi.org/10.1130/g32348.1

Tappe, S., Stracke, A., van Acken, D., Strauss, H., & Luguet, A. (2020). Origins of kimberlites and carbonatites during continental collision—Insights beyond decoupled Nd-Hf isotopes. *Earth-Science Reviews*, *208*, 103287. https://doi.org/10.1016/j.earscirev.2020.103287

Thybo, H., & Artemieva, I. M. (2013). Moho and magmatic underplating in continental lithosphere. *Tectonophysics*, *609*, 605–619. https://doi.org/10.1016/j.tecto.2013.05.032

Tinguely, C. E., Grégoire, M., & le Roex, A. P. (2008). Eclogite and pyroxenite xenoliths from off-craton kimberlites near the Kaapvaal Craton, South Africa. *Comptes Rendus Geoscience*, *340*(12), 811–821. https://doi.org/10.1016/j.crte.2008.06.006

Woodland, A. B., Gräf, C., Sandner, T., Höfer, H. E., Seitz, H.-M., Pearson, D. G., & Kjarsgaard, B. A. (2021). Oxidation state and metasomatism of the lithospheric mantle beneath the Rae Craton, Canada: Strong gradients reflect craton formation and evolution. *Scientific Reports*, *11*(1), 3684. https://doi.org/10.1038/s41598-021-83261-6

Workman, R. K., & Hart, S. R. (2005). Major and trace element composition of the depleted MORB mantle (DMM). *Earth and Planetary Science Letters*, *231*(1–2), 53–72. https://doi.org/10.1016/j.epsl.2004.12.005

Zhang, C.-C., Sun, W.-D., Wang, J.-T., Zhang, L.-P., Sun, S.-J., & Wu, K. (2017). Oxygen fugacity and porphyry mineralization: A zircon perspective of Dexing porphyry Cu deposit, China. *Geochimica et Cosmochimica Acta*, *206*, 343–363. https://doi.org/10.1016/j.gca.2017.03.013